UNIVERSITY OF
KWAZULU-NATAL

INYUVESI
YAKWAZULU-NATALI

EXPERIMENTAL VERIFICATION OF THE TURBULENT EFFECTS ON LASER BEAM PROPAGATION IN AIR

SHIVAN MICHAEL AUGUSTINE

2014

EXPERIMENTAL VERIFICATION OF THE TURBULENT EFFECTS ON LASER BEAM PROPAGATION IN AIR

by

Shivan Michael Augustine

BSc Hons (Physics)

Submitted in partial fulfillment of the requirements

for the degree of Master of Science in the

School of Chemistry and Physics,

University of KwaZulu-Natal

Pietermaritzburg

11 May 2014

Contents

II PUBLICATIONS

List of Figures

Declaration

This dissertation describes the work undertaken in the School of Chemistry and Physics, University of KwaZulu-Natal (Pietermaritzburg), under the supervision of Dr. N. Chetty, between January 2013 and March 2014. I declare this to be my original work except where due reference and credit is given.

Student: Shivan Michael Augustine

Signature: .....

Date: .....

Supervisor: Dr Naven Chetty

Signature: .....

Date: .....

Acknowledgments

- I wish to thank God for giving me the strength, courage and support throughout my studying years. I am forever and always grateful to you.

- To my esteemed supervisor, Dr. N. Chetty, thank you for your assistance and guidance in this project. I appreciate your patience, kindness and willingness throughout the years to help me.

- Thanks goes to the NRF and CSIR for awarding me scholarships throughout my MSc.

- Mr. Guy Dewar and Mr. Karl Penzhorn are thanked for helping to develop new equipment for my experiment.

- To my amazing wife Eurika Augustine, I appreciate everything you've done for me, thank you for your patience and help with this dissertation.

- Lastly, I wish to extend my gratitude to my closest friends and family, my gran Lalitha Ramdeen, my mother Nishi Rajkumaar and my brother Jashan Augustine for your well wishes, moral support and general interest in my work.

SUMMARY

In this work we have modified and further developed an existing experiment to accurately detect and measure the effects of thermal perturbations on a laser beam propagating through a turbulent medium. This experiment used a high power laser which propagated through, amongst other optical components, a highly sensitive detector called a point diffraction interferometer (PDI). The main modification included the design of a new turbulence delivery system which was able to deliver consistent heating profiles of up to 60°C above room temperature. Other additions were a highly sensitive pressure sensor which measured the slight fluctuations of pressure in the turbulent region. The produced interferograms were analysed using various imaging software. Fast Fourier transforms were applied to the produced interferograms and the results were thus analysed. Analysed data has shown intensity and directional fluctuations to increase with increasing temperature and energy redistributions were evident in the higher temperature regimes. These results have confirmed, within the Kolmogorov regime, that phase and intensity fluctuations increase relative to temperature. The turbulent region exhibited very strong turbulence, in the range $1.1 \times 10^{-12}\,\mathrm{m}^{-2/3}$ to $2.7 \times 10^{-12}\,\mathrm{m}^{-2/3}$. Despite the strong turbulence, the scintillation proved contradictory. It exhibited the condition for a weak turbulent environment (as was determined in the laboratory). It may be inferred that this condition was resultant from the relatively short propagation distances achieved in the laboratory. In the open atmosphere, path lengths extend over vast distances and in order for the turbulent effects to be realised, the turbulence model must generate stronger turbulence. The model was thus able to demonstrate its

ability to fully quantify and determine the thermal turbulence effects on a propagating laser beam. Future work consists of changing the turbulent source to include a heated wind stream which provides heat through a high velocity medium. Also of interest will be to move the entire setup to longer propagation distances in an open environment. A different choice of laser may also be necessary to examine the effect to which other lasers are influenced. Such results are useful in defense weapon technology and are therefore sought after by many researchers.

Thesis Structure

This dissertation consists of five chapters. Chapters one to four collectively describe the theory, experimental techniques and methodologies. The fifth chapter presents a paper submitted and published by the journal ATMÓSFERA on 1 October 2014 in Volume 27-4, titled "Experimental Verification Of The Turbulent Effects On Laser Beam Propagation In Space", which fully describes all experimental results and discussions.

Chapter 1 contains the background theory of the atmosphere, methods of turbulence detection and their applications, an introduction to our proposed method of designing our apparatus.

Chapter 2 presents various turbulence detection methods. A complete description of the point-diffraction interferometer (PDI) is also presented.

Chapter 3 introduces some background on laser beam propagation through the atmosphere and describes the formation of interferograms with particular

emphasis on Gaussian beams.

Chapter 4 presents the theory of perturbed and unperturbed laser beams, Rytov and Kolmogorov theory and the background to obtaining the $C_n^2(h)$ profile. The concept of Fourier transforms applied to image processing is also introduced.

Chapter 5 presents the prepared journal article submitted to ATMÓSFERA in the required format and describes the complete setup required to fully classify the thermal effects on a laser beam propagating in air. New data for the turbulence strength C_n^2, the Rytov variance (scintillation) and the coherence diameter (Fried's parameter) were successfully measured in a laboratory using a point diffraction interferometer.

Appendix A contains the reproduced results from our modified system for obtaining the perturbed interferograms.

Appendix B contains the Mathematica code for the results discussed in Paper 1.

Part I

General Introduction

Chapter 1

INTRODUCTION

1.1 Background

The atmosphere in itself is a refractive medium which varies according to the height profile above ground level. According to Andrews *et al.* [1] and Strohbehm [2], the refractive index fluctuations are significant near the surface of the Earth and negligible at higher altitudes. Fluctuating temperature, humidity and air velocity cause variations, both temporal and spatial, in the refractive index of the atmosphere [3]. Studies have found that a beam can diffract away from the alignment path for an image receiver as well as experience phase perturbations [4]. It should be noted that a laser beam propagating through a medium with a constant refractive index will follow a straight line path from the source to the receiver.

In the atmosphere there are three primary phenomena contributing to optical turbulence. These factors are absorption, scattering and refractive index fluctuations [5, 6]. Absorption and scattering affect the propagation of a laser

beam in the atmosphere as the constituent gases in the atmosphere interact with the beam resulting in an attenuation of the beam [7, 8]. Refractive index fluctuations in the atmosphere lead to beam wander, loss of coherence, beam directional fluctuations and irradiance fluctuations [7–10]. These concepts will be discussed in more detail in Chapter 4.

There are several methods which have been developed for atmospheric turbulence detection. These methods have proven to be successful in their technological applications, notably in the domains of military [11, 12], radar [13], remote sensing [14], satellite communications [15] and medical diagnostics [16, 17]. The military require in-depth knowledge of laser-atmosphere interactions, as it is these factors which inevitably allow for the focusing of military weapons on or off a target. A real life example of such a situation could be the use of long-range lasers for the protection of ships against anti-ship missiles and the protection of aircrafts against surface-to-air missiles during take-off and landing [18]. Radars also make use of long range lasers for remote sensing of both terrestrial and space environments [18]. Satellite communications have been improved with the use of lasers instead of the currently used radio waves as a communication medium for data. Lasers allow for faster data rate transfers when compared to radio waves. This allows for less interruption and better communication over longer distances. In the medical field, high intensity lasers are used for ablation purposes as they introduce a non-invasive technique for removing material such as tumors and cancers from the human body [19–22].

The technology required to model the behaviour of laser beams under turbulent constraints for the aforementioned domains, is extremely expensive, since bulky and fixed positioned apparatus is used. Furthermore, they require state of the art laboratories. It has been shown in recent work that it is fairly difficult to numerical compute the effect of thermal turbulence as shown by Carnevale *et al.* and Bernardini *et al.* [23, 24], who have used the cross spectral density (CSD) method to indicate that turbulence was extremely difficult to measure. In light of the complexity of the other techniques, we will be adopting the method used by Ndlovu [4], as it is a robust and highly sensitive method for determining the effect of atmospheric turbulence on a laser beam propagating through the laboratory. The employed setup utilises a Smart interferometer, also known as a point-diffraction interferometer (PDI). The PDI is capable of accurately detecting and measuring wave-front aberrations [25–27]. PDI's are one of the simplest and lowest cost interferometers and are useful for describing variations in phase differences as slight variations in fringe positions [28]. Such a capability allows comparisons to be made between the produced perturbed and unperturbed interference patterns. The apparatus setup requires the PDI to be positioned just before the detector (in this case a DSLR camera). The laser beam enters the PDI through a small pinhole, located on an absorbing film, of adjustable size and tilt. Some of the light from the Point Spread Function (PDF) is diffracted through the pinhole giving rise to a spherical wavefront. A copy of the original, distorted wavefront also gets through the plate and interferes with the reference wavefront emanating from the pinhole [27, 28]. Kolmogorov [29] and Strohbehn [30]

have classified parameters of the optical turbulence by the outer scale L_0, the inner scale l_0 and the refractive index structure coefficient C_n^2. The structure coefficient alone provides adequate information about the turbulent region and typically ranges from $10^{-17}\mathrm{m}^{-2/3}$ or less for weak turbulences and $10^{-13}\mathrm{m}^{-2/3}$ or more for strong turbulence, with $10^{-15}\mathrm{m}^{-2/3}$ being the average value [1, 31, 32]. Data extrapolated from the interferograms can be useful when characterising the energy distribution, intensity profile and phase changes.

For the purposes of this work, we have chosen a TEM_{00} He-Ne laser as the light source. The choice of laser is a fundamental step in the experimental design since the results rely greatly on a consistent intensity profile. To achieve reproducible results, a stable He-Ne 0.532 micron laser has been used and this will be discussed in further detail on page 62. The turbulence delivery has been optimised in which a new design has been employed over the previous cigarette lighter method used by Ndlovu [4]. The model incorporates using an aluminum panel with multiple high powered resistors arranged on the underside to provide consistent heating above. A full description is provided in on page 64. Lastly, the collimating lenses and filters have been polished and cleaned. The details of the collimators are described in on page 63. These modifications shall in essence provide more stable and reliable results.

References

[1] Andrews L. C. & Phillips, R. L., 2005. *Laser Beam Propagation Through Random Media*, SPIE Press, USA.

[2] Strohbehm J. W., 1978. "Laser Beam Propagation In The Atmosphere", New York, Springer-Verlag.

[3] Wesley M. L., 1976. "The Combined Effect of Temperature and Humidity Fluctuations on Refractive Index", *American Meteor. Soc. J.*, 15, 43-49.

[4] Ndlovu S., 2013. "Experimental Measurement of the Fluctuations of Laser Beam Due to Thermal Turbulence", MSc thesis, Dept. of Chemistry and Physics, University of Natal.

[5] Bohren C. & Huffman D., 1983. "Absorption and Scattering of Light by Small Particles", John Wiley and Sons, Republic of Germany.

[6] Fernndez M. M., Vilnrotter A. V., Mukai R. and Hassib B., 2006. "Coherent Optical Array Receiver Experiment: Design, implementation and BER performance of a multichannel coherent optical receiver for PPM

signals under atmospheric turbulence", *Free-Space Laser Communication Technologies XVIII*, Proc. SPIE, 6105.

[7] Isterling W. M., 2010. *Electro-Optic Propagation Through Highly Aberrant Media*, Phd Thesis, University of Adelaide, Australia.

[8] Shaik K. S, 1988. "Atmospheric Propagation Effects Relevant to Optical Communications", *TDA Progress Report*, 180-188.

[9] Yuksel H., 2005. *Studies of the Effects of Atmospheric Turbulence on Free Space Optical Communications*, PhD Thesis, University of Maryland, United States.

[10] Berman G. P., Chumak A. A. and Gorshkov V. N., 2013. *Beam Wandering in the Atmosphere:The Effect of Partial Coherence*, Los Alamos National Laboratory, Institute of Physics of the National Academy of Sciences, Ukraine.

[11] Titterton D. H., 2006. "The Development of Infrared Countermeasure Technology and Systems", *Mid IR Semiconductor Optronic*, Springer London, 635-671.

[12] Consortini A. & O'Donnell K. A., 1991. "Beam Wandering of Thin Parallel Beams Through Atmospheric Turbulence", *Waves in Random Media*, 3, 11-28.

[13] Mead J. B. & McIntosh R. E., 1990. "Millimeter-wave polarimetric radars", *Progress In Electromagnetics Research*, PIER 03, 391-450.

[14] Shin R. T. & Kong J. A., 1989. "Radiative transfer theory for active remote sensing of two-layer random medium", *Progress In Electromagnetics Research*, PIER 01, 359-417.

[15] Ojo J. S., Ajewole M. O. and Sarkar S. K., 2007. "Rain rate and rain attenuation prediction for satellite communication in Ku and Ka bands over Nigeria", *Progress In Electrodynamics Research B*, 5, 207-223.

[16] Lonappen A., Bindu G., Thomas V., Jacob J., Rajasekaran C. and Mathew K. T., 2007. "Diagnosis of Diabetes Mellitus Using Microwaves", *Journal of Electromagnetic Waves and Applications*, 21, 10.

[17] Ibrahim A. T., 2007. "Using Microwave Energy To Treat Tumors", *Progress In Electromagnetic Research B*, 3, .1-27.

[18] Socol Y., 2012. "High-power Free-electron Lasers-technology and Future Applications", *Optics and Laser Technology*, 46, 124-125.

[19] Hartary P., 1997. *Ballistic Missile Defense Organization*, Diane Publishing Company, Virginia.

[20] Marsh R. de W. and Samuel J., 2005. *Clinical Oncology*, Jaypee Brothers Medical Publishers (P) Ltd, India.

[21] Hicks R., 2009. *Understanding Cancer*, Second Ed., Southwood Press Pty Ltd., Brisbane.

[22] Rai A. K., Das I. M. K., Uttam K. N. (eds), 2009. *Emerging Trends in Laser & Spectroscopy and Applications*, Sunil Sachdev, New Delhi.

[23] Carnevale M., Montomoli F., D'Ammaro A., Salvadori S., Martelli F., 2013. "'Uncertainty Quantification: A Stochastic Method for Heat Transfer Prediction Using LES', *ASME J. Turbomach*, 135, 051021.

[24] Bernardini C., Carnevale M., Salvadori S., Martelli F., 2011. "On the Assessment of an Unstructured Finite-Volume DES/LES Solver for Turbomachinery Applications", *WSEAS Transactions on Fluid Mechanics*, 6, 160-173.

[25] Furuhashi H., Shibata A., Uchida Y., Matsuda K., and Grover C. P., 2004. "A point diffraction interferometer with random-dot filter," *Opt. Comm.*, 273, 17-24.

[26] Aggarwal A. K. & Kaura S. A., 1986. "Further applications of point diffraction interferometer," *J. Opt.*, 17(3), 135-138.

[27] Naulleau P. P., Goldberg A. K., Lee H. S., Chang C., Attwood D. and Bokor J., 1999. "Extreme-ultraviolet phase-shifting point-diffraction interferometer: a wave-front metrology tool with subangstrom reference-wave accuracy", *Appl. Opt.*, 38, 7252-7263.

[28] Smartt R. N. & Steel W. H., 1975. "Theory and Application of Point-diffraction Interferometers", *Japan. J. appl. Phys.*, 14, 1-41.

[29] Kolmogorov A. N. 1991. "The local Structure of Turbulence in Incompressible Viscous Fluid for Very Large Reynolds Numbers", *Proceedings: Mathematical and Physical Sciences*, 434, 9-13.

[30] Strohbehn J. W. & Clifford S. F., 1978. *Laser Beam Propagation in the Atmosphere*, Springer-Verlag, New York.

[31] Majumdar, A. K., 2005. "Free-space laser communication performance in theatmospheric channel", *J. Opt. Fiber Commun. Res.*, 2, 345396.

[32] Weichel H., 1990. *Laser Beam Propagation in the Atmosphere*, SPIE, USA.

Chapter 2

TURBULENCE DETECTION METHODS

2.1 SCIDAR - Scintillation detection and ranging

SCIDAR was developed by Vernin and Roddier [1] in 1973 and has proved to be an extremely effective method of determining the optical vertical structure of the atmospheric turbulence strength. SCIDAR is a remote sensing technique which is used to measure $C_n^2(h)$, which as previously mentioned is the structure constant of the atmospheric refractive index relative to height. This method provides a direct measure of the vertical turbulence profile, and although it works well over long propagation distances ($\geq 1\,\mathrm{km}$), it fails for short propagation distances since the scintillation variance is barely detectable [2, 3]. The method is better suited to capturing a large number of binary star scintillation patterns and hence the calculation of the average scintillation autocovariance in real time [2,3]. The refractive

index parameter $C_n^2(h)$ is related to the scintillation autocovariance by [4],

$$S(\rho) = T(\rho, h)C_n^2(h) + n(\rho), \tag{2.1}$$

where ρ is the physical distance in the measurement plane, $T(\rho, h)$ is the theoretical autocovariances for a wide range of altitudes, $S(\rho)$ is the normalised average scintillation covariance determined from the observed scintillation frames and $n(\rho)$ is the measurement noise [4].

Generalised SCIDAR provides sufficient information of $C_n^2(h)$ which in turn provides essential parameters such as the seeing conditions (ϵ), the atmospheric coherence diameter (called Fried's seeing parameter) (r_0), coherence lengths and time of the wave fronts. Fried's parameter is related to $C_n^2(h)$ by [5],

$$r_0 = 0.185 \left[\frac{\bar{\lambda}^2}{\int_0^z C_n^2(h)dh} \right]^{3/5}, \tag{2.2}$$

and is a measure of the quality of the optical signal through the atmosphere. Typical values of r_0 at a good observatory point range between 5 to 20 cm and depend largely on the seeing conditions [5]. The highly stochastic nature of the atmosphere determines the seeing strength. At ground level, the convective nature of the atmosphere imposes strong turbulence which can lead to poor seeing conditions. Since atmospheric turbulence exists to about 20 km above the earth, good seeing conditions can be located on mountain tops where turbulent effects are relatively weak [5].

2.2 SLODAR - Slope detection and ranging

SLODAR is a turbulence detection method which makes use of Shack-Hartmann wavefront sensors (SHWFS) to determine the vertical distribution of atmospheric optical turbulence [6, 7]. The first use of the (SHWFS) was to measure the turbulence profiles by the Centre for Advanced Instrumentation (CfAI), Durham at the Observatorio del Roque de los Muchachos, La Palma [8]. Most SLODAR systems make use of single (SHWFS) to measure the wavefront slopes from binary stars [7]. Further applications of SLODAR involved astronomical adaptive optics as well as free space optical communications [9–11]. The general experimental SLODAR technique is as follows, two telescopes each emitting a parallel beam are placed closed to each other and are focused at two point sources which are separated by a small angle [9,10]. These point sources could be stars for the astronomical case. Each beam is analysed by a (SHWFS). Determining the wavefront gradients of the beam, allows for the calculation of the integrated turbulence strength along the path length [11]. Further information can be established by measuring the cross correlations between the slope patterns from the sources such as the location of the turbulence and the wind speed [9].

2.3 LIDAR - Light detection and ranging

LIDAR is a remote sensing technique used to provide range resolved or integrated measurements of particularly high accuracy and resolving power [12–16]. The LIDAR system is relatively modern in the field of geospatial modeling [12,13,17]. The unique

design incorporates a laser scanning system, a ground positioning system (GPS) and a inertial measuring unit (IMU) [17]. The IMU is applicable when it is being used on an aircraft. The range measurements between two reference points are obtained by the laser scanner [17]. While the system is able to take measurements in open textureless plains, it fails when the laser beam experiences phase and amplitude fluctuations, additionally obstructions such as smoke, fog and cloud cover disrupt imaging and tracking capabilities [17, 18].

It has been shown by Zilberman [19] and Kopeika [20] that LIDAR can be used to determine optical turbulence. The equipment can be successfully used to operate over long ranges but is bulky, complex and expensive, which makes deployment very limited. The operating principle is therefore not ideal for near-ground work.

2.4 Scintillometry

The most common method for measuring turbulence strength is optical scintillometry [21]. Scintillometers measure the light intensity scintillations of a horizontally propagating beam. The scintillation occurs due to phase distortions of a laser beam propagating through an inhomogenous medium along a sufficiently long distance. In spite of the initially coherent, on-axis Gaussian beam, propagation over long distances under the constraint of turbulence causes the laser beam to propagate off-axis and to become partially coherent [22, 23]. Evaluation of the average intensity

profile under turbulent conditions, at the receiver is found by Baykal *et al* [24] to be,

$$\langle I(\mathbf{p}{=}\mathbf{0}, L)\rangle = \frac{(0.5k|A|/L)^2 \times \exp\left(-\frac{0.5}{B_2}\left[V^* - \frac{V}{B_1}\left(\frac{1}{\rho_0^2} + \frac{1}{4\rho_s^2}\right)\right]\right)^2 \times \exp\left(-\frac{0.5V^2}{B_1}\right)}{\left[|B_1|^2 - \left(\rho_0^2 + \frac{1}{4\rho_s^2}\right)^2\right]}, \tag{2.3}$$

where,

$$B_1 = \frac{1}{2\alpha_s^2} + \frac{1}{4\rho_s^2} + \frac{1}{\rho_0^2} - \frac{jk}{2L} \qquad \text{and} \qquad B_2 = B_1^* - \frac{1}{B_1}\left(\frac{1}{4\rho_s^2} + \frac{1}{\rho_0^2}\right)^2.$$

The definitions of the variables used in equation (2.4) are provided by Baykal *et al* [24] as,

- $\mathbf{p} = (p_x, p_y)$ are the transverse source and receiver coordinates,
- A is the complex amplitude,
- $j = (-1)^{1/2}$,
- L is the length which the beam propagates,
- $k = \dfrac{2\pi}{\lambda}$ is the wave number,
- V^* is the conjugate of the complex displacement parameter,
- ρ_s is the measure for the degree of coherence reflecting source partial coherence, and
- $\rho_0 = (0.545C_n^2k^2L)^{-3/5}$ is the coherence length.

The scintillation index can be calculated according to [24],

$$\sigma_I^2 = \left[\left\langle I^2(\mathbf{0}, L)/I(\mathbf{0}, L)\right\rangle^2\right] - 1, \tag{2.4}$$

where,

$$I^2(\mathbf{0}, L) = \sum_{n=1}^{3} Y_n. \tag{2.5}$$

The complete expression for Y_n is derived in [24]. Recalling from equation (4.7) that the Rytov variance is directly related to the refractive index structure parameter C_n^2 by [25],

$$\sigma_R^2 = 1.23\, C_n^2\, k^{\frac{7}{6}}\, L^{\frac{11}{6}}. \tag{2.6}$$

2.5 Meteorological air balloons

The measurement of the refractive index structure parameter $C_n^2(h)$ in air is achieved by sending meteorological balloons equipped with temperature sensors high into the atmosphere [26]. The sensors are able to determine the temperature fluctuations $C_T^2(h)$ and relate it to the structure parameter. The advantage is that this method is simple yet effective. The disadvantage is that the profiles take several hours to obtain which can become monotonous [26]. Weather changes are also constraining factors since bad weather can affect the periods results rendering them null and void.

2.6 The point diffraction interferometer

Amongst other devices used for measuring phase variations, the point diffraction interferometer is an optically advanced precision instrument designed in 1933 by Linnik [27] and improved upon by Smartt & Steel [28] in 1975. The PDI boasts numerous advantages over other designs by being cost efficient, small in size, light in weight, highly sensitive and easy aligned. Some of these factors are attributed to the

common path design of the PDI resulting in highly stable interferograms. Various other applications of the PDI have been discussed in the works of Love *et al* [29] and Yu *et al* [30]. The manufacture of a PDI consists of an absorbing layer on a clear substrate with a pin hole which has a size less than that of an Airy disk produced by the original wave subject to no aberrations [31, 32].

2.6.1 General theory of the PDI

In Figure (2.1), the incident wave produced by a laser beam is transmitted through the absorbing film with a reduced amplitude and a spherical wave is produced due to a discontinuity caused by the pinhole [33]. By varying the position of the pin hole, the amount of light can be controlled hence adjusting the number of fringes produced in the interferogram. The sum of the respective complex amplitudes yields a Fourier transform of the amplitude image from the wave plus a δ-function.

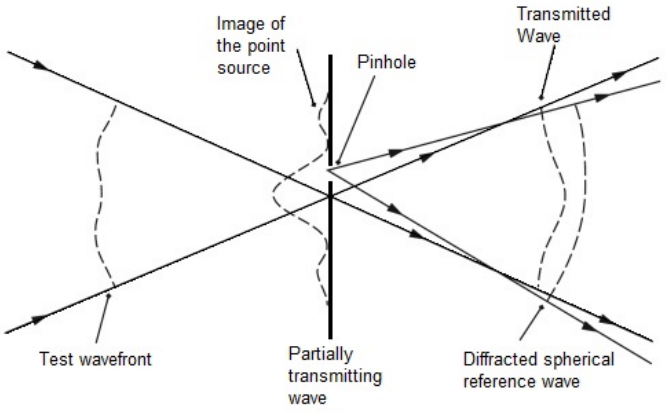

Figure 2.1: The point diffraction interferometer [33].

The general theory for a PDI can be described using Figure (2.2) where, there are 4 planes, namely the source, object, pupil and image [28]. Each plane is represented by the vectors $\mathbf{u}$, $\mathbf{x}$, $\mathbf{u}'$ and $\mathbf{x}'$. Vectors $\mathbf{x}$ and $\mathbf{x}'$ have units of length which represent

the radii of the object and image fields respectfully and are assumed to be circular. Vectors $\mathbf{u}$ and $\mathbf{u}'$ are the actual distances in the planes which have the usual diffraction units of $(2\pi/\lambda)$ [28].

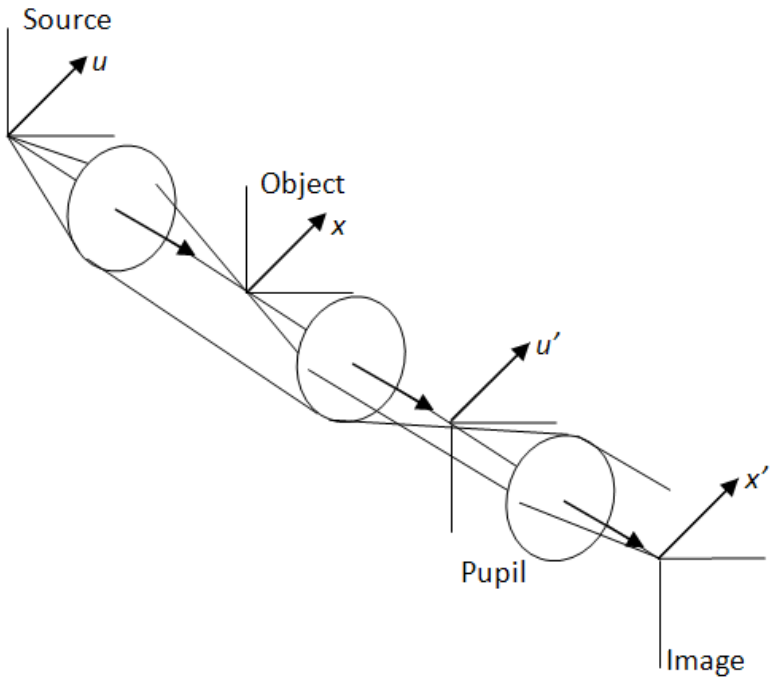

Figure 2.2: Representation of general theory [28].

The Fourier transform that represents Fraunhofer diffraction is then [28],

$$F(\mathbf{x}') = \frac{1}{2\pi} \int \int_{-\infty}^{\infty} f(\mathbf{u}) \exp(-\mathrm{i}\mathbf{u} \cdot \mathbf{x}) \mathrm{d}\mathbf{u}, \tag{2.7}$$

where $F(\mathbf{x}')$ represents the Fourier transform and $f(\mathbf{u})$ is the function. The amplitude $e^{-i\mathbf{u}\cdot\mathbf{x}}$ is taken to have an amplitude transmittance of Smartt and Steel [28],

$$L(\mathbf{x}') = \exp\left[(\mathrm{i}\psi\mathbf{x})\right], \tag{2.8}$$

which only has phase variations. The resulting amplitude at the pupil is then $l(\mathbf{u}'-\mathbf{u})$.

The transmitting filter positioned at the pupil has an amplitude transmittance given by the following as described by Smartt [28],

$$t_1 p(\mathbf{u}') + t_2 g(\mathbf{u}' - \mathbf{U}'), \tag{2.9}$$

where t_1 and t_2 are constants, p($\mathbf{u}'$) represents a function for the full aperture and g($\mathbf{u}'$) represents the function for the diffracting aperture of the pupil, the tilt is given by $\mathbf{U}'$. A the image plane, the complex amplitude is described by Smartt [28] as,

$$A(\mathbf{x}') = t_1 A_p(\mathbf{x}') + t_2 A_g(\mathbf{x}')\exp(-\mathrm{i}\mathbf{U}' \cdot \mathbf{x}'), \tag{2.10}$$

where A_p and A_g represent the amplitude images of the apertures. For a large pupil, we can write [28],

$$A_p(\mathbf{x}') \approx L(\mathbf{x}')\exp(-\mathrm{i}\mathbf{u}' \cdot \mathbf{x}'), \tag{2.11}$$

the formed image has a uniform amplitude as well as equivalent phase variations as the object. For the case of $A_g(\mathbf{x}')$, the amplitude is uniform but has a different phase [28].

The interference of this source point is the squared modulus of equation (2.10). For the whole source, it is assumed to be incoherent and is the integral of this interference over g($\mathbf{u}$) [28],

$$B(\mathbf{x}') = |t_1|^2 + |t_2|^2 + 2\mathrm{Re}\{t_1 t_2^* L(\mathbf{x}')M^*(\mathbf{x}') \times \exp(-\mathrm{i}\mathbf{U}' \cdot \mathbf{x}'\}, \tag{2.12}$$

where Re is the real part, * the complex conjugate and

$$M(\mathbf{x}') = \frac{1}{2\pi} \int \int_{-\infty}^{\infty} |G(\mathbf{x}' - \mathbf{x})|^2 L(\mathbf{x}) \times \exp(-\mathrm{i}\mathbf{U}' \cdot \mathbf{x}') \mathrm{d}\mathbf{x}, \tag{2.13}$$

with $G(\mathbf{x}')$ being the transformation of g($\mathbf{u}$).

2.6.2 PDI design

The PDI plate is manufactured by Astro Electronics and is shown in Figure (2.3).

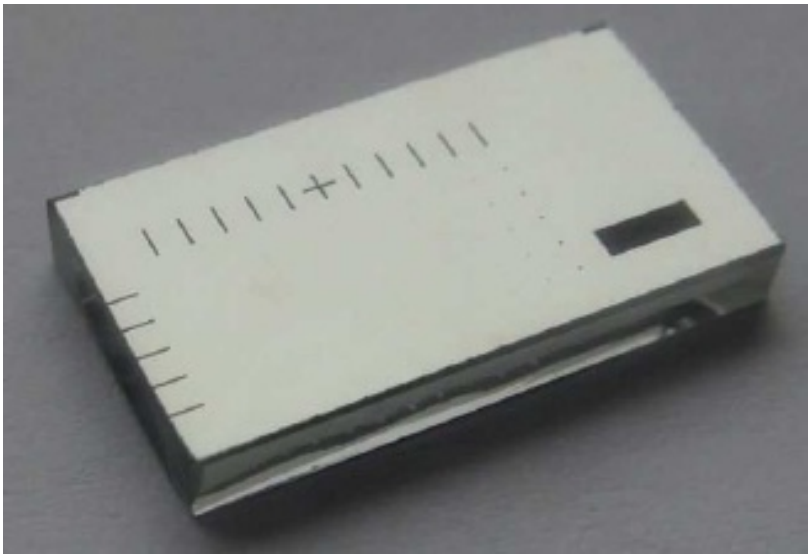

Figure 2.3: The PDI plate

The layout of the pinholes on the PDI is shown in Figure (2.4). The pinholes are distributed on an array of pitch 1 mm. It is therefore possible that simple doublets will serve the required purposes in all cases.

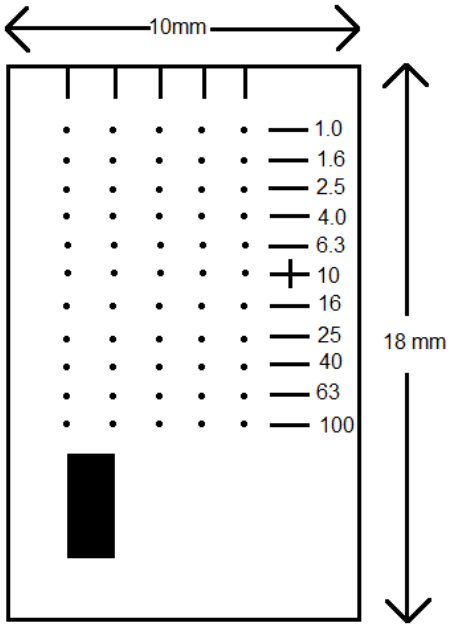

Figure 2.4: Layout of pinholes on PDI plate.

The PDI carrier cell is an Edmund XYZ stage. The PDI plate is coloured in yellow and is recessed into the cell to help provide protection, but is still vulnerable to contamination. When not in use, the PDI is covered to protect it from dust.

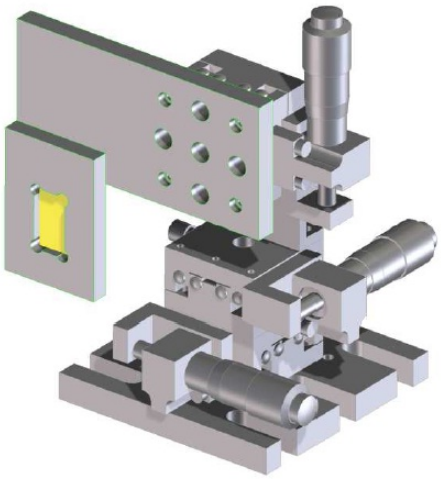

Figure 2.5: Edmund XYZ stage with PDI and carrier cell.

References

[1] Vernin J. & Roddier F., 1973. "Experimental determination of two-dimensional spatiotemporal power spectra of stellar light scintillation", *J. Opt. Soc. Am.*, 63, 270-273.

[2] Avila R., Vernin J., & Masciadri E., 1997. "Whole Atmospheric-Turbulence Profiling with Generalized Scidar", *Appl. Opt.*, 3, p.7898-7905.

[3] Hippler S., 2007, "A Generalized SCIDAR Facility for the LBT", viewed 28 January 2014, from http://www.mpia-hd.mpg.de/ao/atmosphere/scidar/scidarintro.html

[4] Millerd J. E., Brock N. J., Hayes J. B. & Wyant J. C., 2004. "Instantaneous phase-shift, point-diffraction interferometer", *Proc. SPIE*, 5531, 264-272.

[5] Magee E. P., 1993. *Characterisation of Laboratory Generated Turbulence*, MSc Thesis, Air Force Institute of Technology, United States.

[6] Wilson R. W., 2002. "SLODAR: Measuring Optical Turbulence Altitude with a Shack Hartmann Wavefront Sensor", *Mon. Not. R. Astron. Soc.,* 337, 103-108.

[7] Butterley T., Wilson R. W. & Sarazin M., 2006. "Determination of The Profile of Atmospheric Optical Turbulence Strength From SLODAR Data", *Mon. Not. R. Astron. Soc.*, 369, 789-845.

[8] Wang L., Schöck M. & Chanan G., 2008. "Atmospheric turbulence profiling with slodar using multiple adaptive optics wavefront sensors", *Appl. Opt.*, 47(11), 1880-1892.

[9] Love G. D., Dunlop C. N., Patrick S., Saunter C. D., Wilson R. W. & Wright C., 2005. "Horizontal Turbulence Measurements using SLODAR", *In Optics & Photonics 2005*, 589104-589104.

[10] Jolissaint L., Keskin O., Bradley C., Wallace B. & Hilton A., 2004. "Multiple-layer Optical Turbulence Generator Principle and SLODAR Characterization: Preliminary results", *Optics in Atmospheric Propagation and Adaptive Systems VII*, *Proc.SPIE*, 5572, 256-261.

[11] Wilson R. W., Bate J., Guerra J. C., Hubin N. N., Sarazin M. & Saunter C. D., 2004. "Development of a Portable SLODAR Turbulence Profiler", *Advancements in Adaptive Optics*, 5490, 758-765.

[12] Sun G., Ranson K. J., Kharuk V. I. & Kovacs K., 2003. "Validation of Surface Height from Shuttle Radar Topology Mission Using Shuttle Laser Altimeter," *Remote Sensing of Environment*, 88, 401-411.

[13] Lefsky M. A., Harding D. J., Keller M., Cohen W. B., Carabajal C. C., Del Bom Espirito-Santo F., Hunter M. O. & de Oliveira Jr. R., 2005. "Estimates of

Forest Canopy Height and Aboveground Biomass Using ICESat", Geophysical Research Letters 32, L22S02. doi:10.1029/2005GL023971.

[14] Hofton M., Dubayah R., Blair J. B. & Rabine D., 2006. "Validation of SRTM Elevations Over Vegetated and Non-Vegetated Terrain Using Medium Footprint Lidar", *Photogrammetric Engineering & Remote Sensing*, 72(3), 279-285.

[15] Chen Q., 2007. "Airborne Lidar Data Processing and Information Extraction", *Photogrammetric Engineering & Remote Sensing*, 73(2), 109-112.

[16] Simard M., Rivera-Monroy V. H., Ernesto Mancera-Pineda J., Castaneda-Moya E. & Twilley R. R., 2008. "A Systematic Method for 3D Mapping of Mangrove Forests Based on Shuttle Radar Topology Mission Elevation Data, ICEsat/GLAS waveforms and field data: Application to Cienaga Grande de Santa Marta, Colombia", *Remote Sensing of Environment*, 112(5), 2131-2144.

[17] Tiwari P. S. & Pande H., LIDAR Remote Sensing Applications in Automated Urban Feature Extraction.

[18] Liu B., (2006), *Optimal Beam Forming for Laser Beam Propagation Through Random Media*, MSc Thesis, Michigan Technological University, USA.

[19] Zilberman, A. & Kopeika N. S., 2004. "LIDAR measurements of atmospheric turbulence vertical", *Free-Space Laser Communication Technologies XVI*, 5338(1), 288-297.

[20] Zilberman, A. & Kopeika, N. S., 2008. "Laser Beam Wander in the Atmosphere: Implications for Optical Turbulence Vertical Profile Sensing with Imaging LIDAR", *Journal of Applied Remote Sensing*, 2(1), 023540-023540.

[21] Poggio P. L., Furger M., Prevot H. S. A. & Graber K. W., 1999. "Scintillometer Wind Measurements over Complex Terrain", *Journal of atmospheric and oceanic technology*, 1-5.

[22] Milonni P. W. & Eberly J. H., 2010. *Introduction to Laser Operation*, John Wiley & Sons, Inc., USA.

[23] Casperson L. W., 1973. "Gaussian Light Beams in Inhomogeneous Media", *Appl. Opt.*, 12, 2434-2441.

[24] Baykal Y., Eyyubolu H. T. & Cai Y., 2010. "Partially Coherent Off-Axis Gaussian Beam Scintillations", *Journal of Modern Optics*, 1221-1227.

[25] Andrews L. C. & Phillips, R. L., 2005. *Laser Beam Propagation Through Random Media*, SPIE Press, USA.

[26] Azouit M. & Vernin J., 2005. "Optical Turbulence Profiling With Balloons Relevant to Astronomy and Atmospheric Physics", PASP.

[27] Mercer C. R. & Creath K., 1994. "Liquid crystal point-diffraction interferometer", *Optics Letters*, 19(12), 916-918.

[28] Smartt R. N. & Steel W. H., 1975. "Theory and Application of Point-diffraction Interferometers", *Japan. J. appl. Phys.*, 14, 14-21.

[29] Love G. D., Oag T. J. & Kirby A. K., 2005. "Common path interferometric wavefront sensors for extreme adaptive optics," *Optics Express*, 13, 3491-3499.

[30] Yu Z., Chunsui J. & Dongmei M., 2012. "Analysis of air turbulence errors for visible light phase shifting point diffraction interferometer," *Infrared and Laser Engineering*, 41, 1899-1904.

[31] Maracara D. (ed), 2007. *Optical Shop Testing*, 3rd ed., John Wiley & Sons, Inc., Canada.

[32] Kadono H., Ogusu M. & Toyooka S., 1994. "Phase shifting common path interferometer using a liquid-crystal phase modulator", *Opt. Commun.*, 110, 391-400.

[33] Ferraro P., Paturzo M. & Grilli S., 2007. Optical Wavefront Measurement Using a Novel Phase-Shifting Point-Diffraction Interferometer.

Chapter 3

ATMOSPHERIC OPTICS

The atmosphere, see Figure (3.1), comprises of three layers with each having their own unique properties [1]. The troposphere describes our region of interest since it is the most active in terms of wind sheer, humidity and displays a consistent decrease in temperature with respect to altitude. Most weather changes occur within the troposphere and lower stratosphere. Particles in the air are composed of dust, salt crystals and other combustion elements [2]. The interference effect of these particles on a laser beam propagating through it depends on the water content of the air. Changing temperature and pressure cause random temporal and spatial fluctuations in the refractive index of the atmosphere. The inconsistencies arising from various refractive index changes can be described by turbulent eddies. Each turbulent eddy has a respective size and a unique refractive index characteristic. The smallest turbulent eddy size is distinguished by the inner scale l_0 and the largest, known as the outer scale, by L_0 [3].

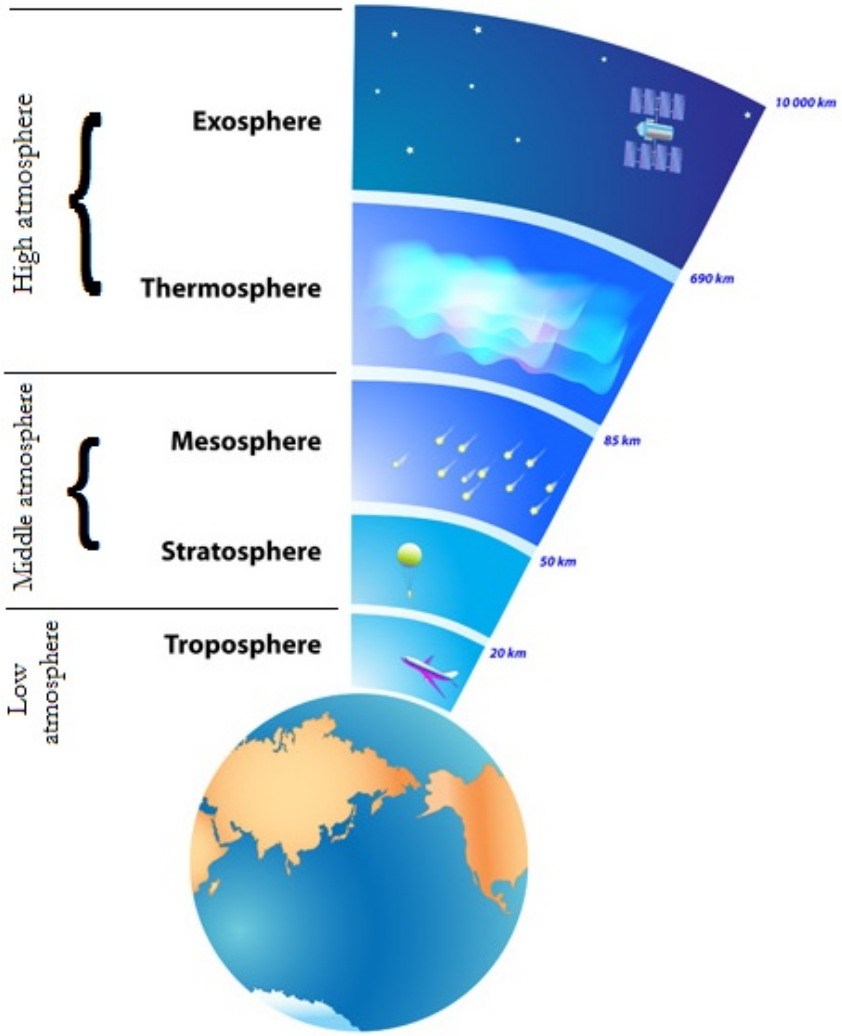

Figure 3.1: Layers of the atmosphere [1].

3.1 Laser beam propagation in air

A Gaussian, monochromatic laser beam propagating horizontally through a turbulent zone will experience phase perturbations due to random refractive index fluctuations of the atmosphere. For a single turbulent layer, the complex field is described by Roddier [4] as,

$$\psi_h(\mathbf{r}) = e^{i\phi(\mathbf{r})}, \tag{3.1}$$

where $\mathbf{r}$ is a vector coordinate in space at altitude h above the ground and $\phi(\mathbf{r})$ is the phase variations caused by the random index variations $n(\mathbf{r}, h)$. Assuming that the turbulent region is a thin layer of width δh, the phase variation can be written as [4],

$$\phi(\mathbf{r}) = k \int_{h}^{h+\delta h} dz\, n(\mathbf{r}, z), \tag{3.2}$$

where $k = \dfrac{2\pi}{\lambda}$.

3.2 Interferograms

Interferograms are formed once the laser beam has propagated through a series of optical components. The incident wave is transmitted through the absorbing film with a reduced amplitude and a spherical reference wave is produced due to the point discontinuity at the pinhole [5]. By adjusting the position of the pinhole, the amount of light entering the PDI can be controlled. The spherical reference wave is thereafter recombined with the transmitted wave to interfere [5]. Interference is constructive at numerous wavelength points and destructive at others. Formed interferograms are captured using a relatively high quality DSLR camera. As with any interferogram, it is then necessary to extract object wavefront information. Due to the PDI's common path design, measuring the shift in phase of one beam relative to another beam is difficult. Attempts to amalgamate phase-shifting (PS) interferometry have been discussed in [6–9]. Various software is available for fringe analysis such as Durango, Matlab, OpenFringe and ImageJ. On comparison of a few freeware options, Matlab and imageJ proved to be the software of choice since they allowed for a wide range

of interferogram analysis.

3.3 Gaussian beams

Most common laser beams and more specifically, the laser used in this work, have Gaussian intensity profiles. A Gaussian beam is chosen since the energy distribution is uniform and minor perturbations to the laser beam are displayed in the perturbed intensity profile. The Gaussian intensity profile can readily be seen from the interference pattern of an unperturbed laser beam as in Figure (3.2).

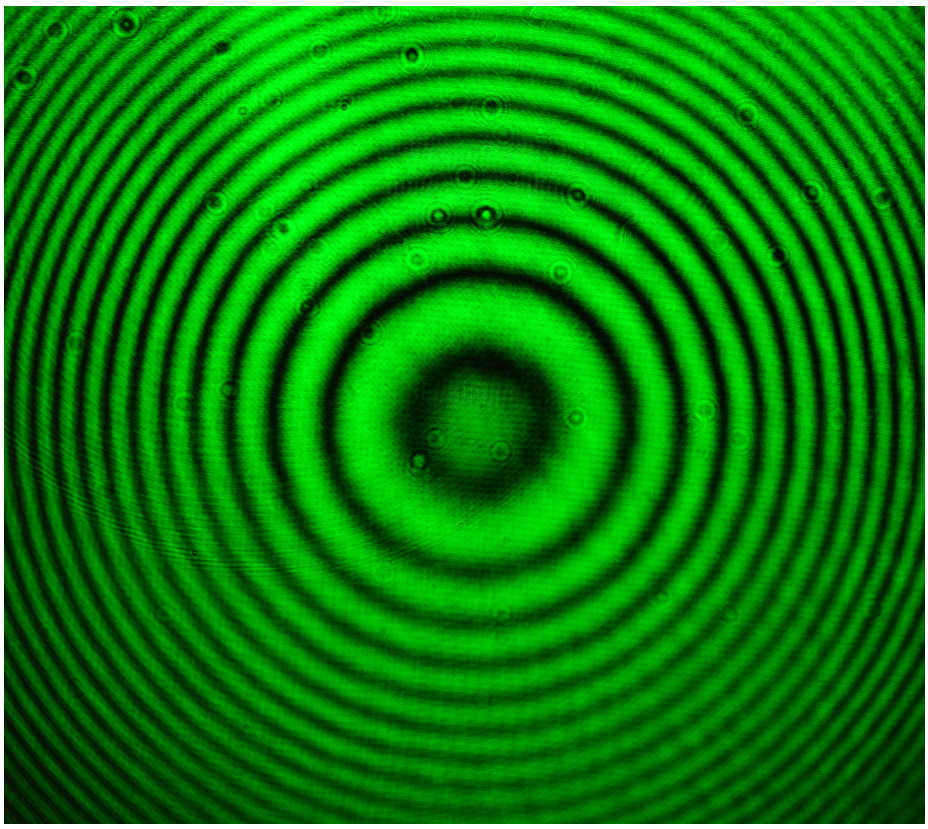

Figure 3.2: Interferogram of the unperturbed laser beam.

The surface plot of the unperturbed beam is shown in Figure (3.3). Surface plots are useful when observing the different intensity peaks of an image. The highest intensities are represented by the highest grey values and the lowest intensities are described by the lowest grey values. Figure 3.3 clearly indicates that the centre of Figure 3.2 has the highest intensity. The intensity slowly decreases from the centroid to the edges of the interferogram which according to Figure 3.3, represents the lowest intensity points. This is expected since a Gaussian laser beam is used in this work.

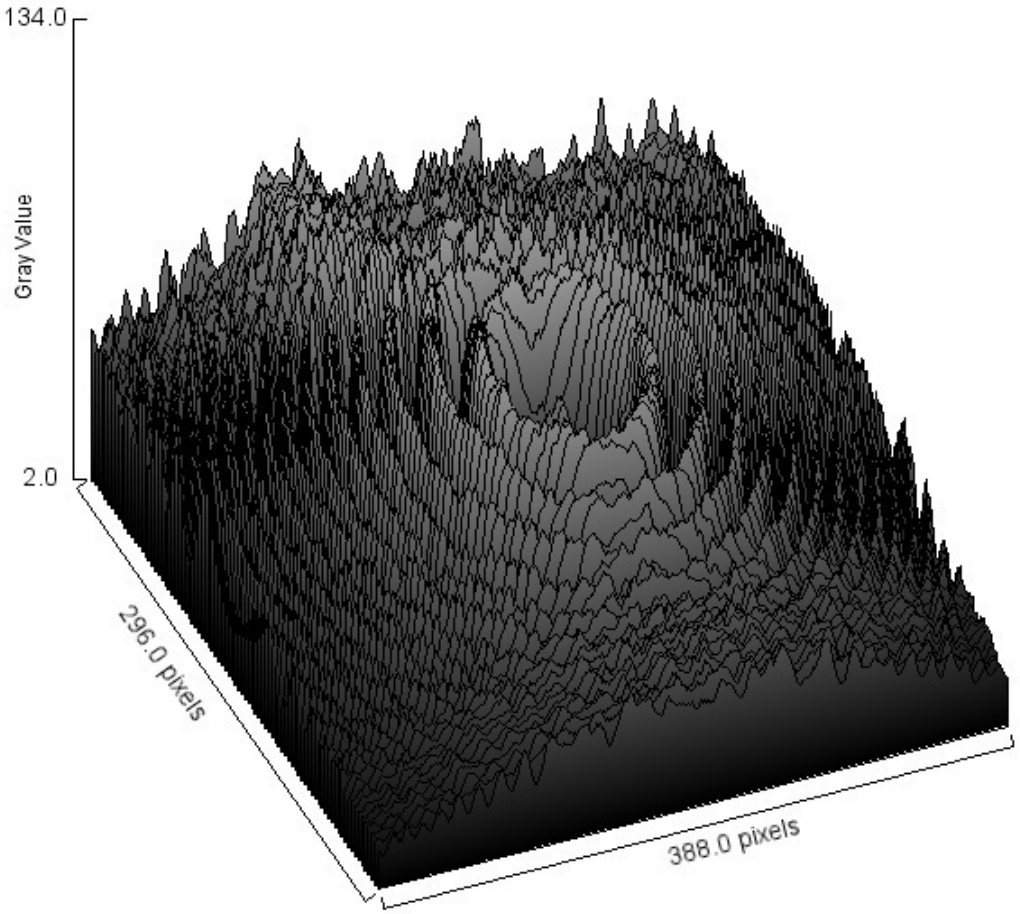

Figure 3.3: Surface plot of the unperturbed laser beam.

Figure (3.4) is an intensity profile of the unperturbed laser beam. The superimposed red line shows the standard form of a Gaussian distribution. The unperturbed

intensity profile follows, to within a good approximation, a Gaussian intensity profile. The central dip could be attributed to attenuation of the laser beam at the point discontinuity of the PDI.

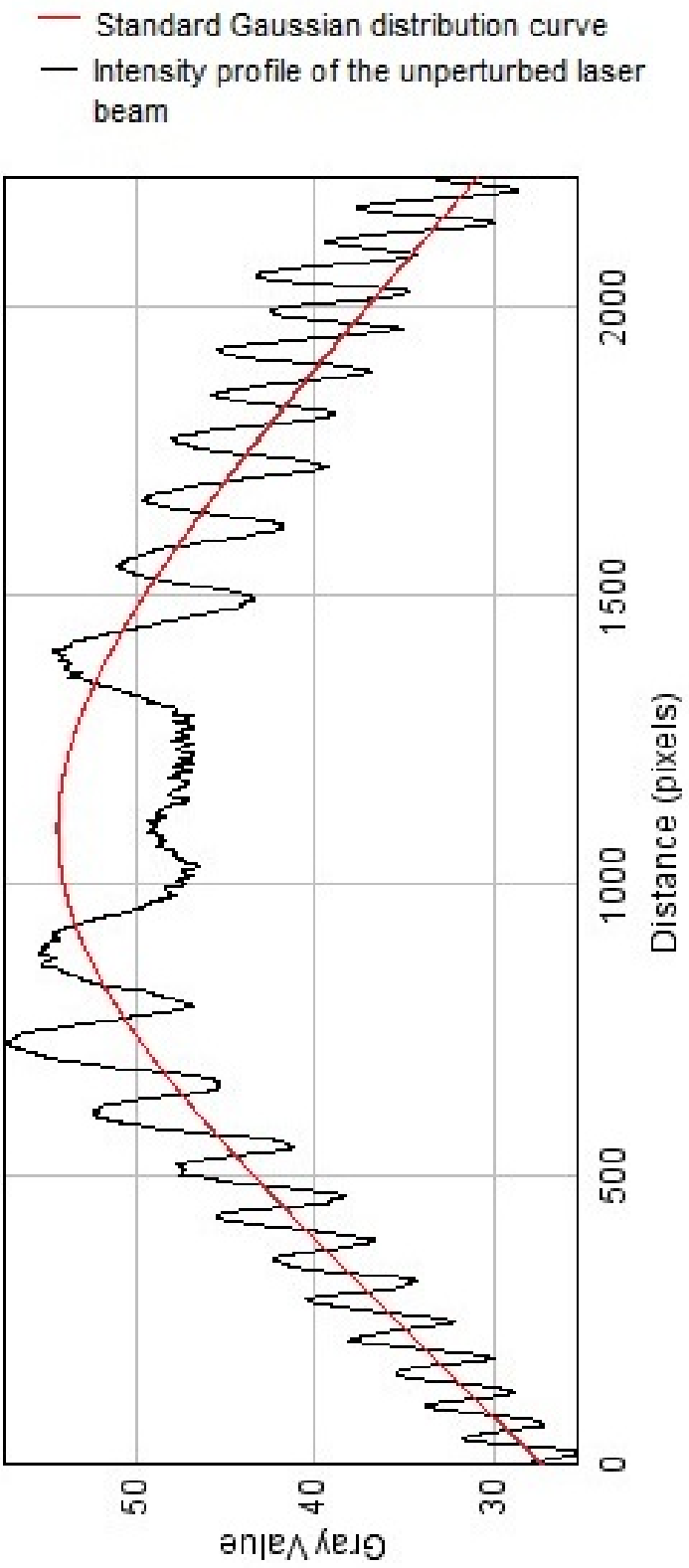

Figure 3.4: Intensity profile of the unperturbed laser beam.

The Gaussian beam is considered to be a transverse electromagnetic wave (TEM_{00}) with a spherical phase front [10]. To understand the propagation of a Gaussian laser beam in air, an understanding of diffraction theory is necessary. Theory tells us that a laser beam propagating in air will diverge away from the source regardless of how parallel the beam is initially [11]. The key characteristics of a propagating Gaussian beam is the beam radius w(z) and the radius of curvature of the phase front R(z) [12]. The beam radius is defined as the transverse distance from the centre of the beam to the point where the intensity has fallen to $1/e^2$ from the centre of the beam [12]. The expressions for these characteristics are [13],

$$\mathrm{w(z)} = \mathrm{w_0}\sqrt{1 + \left(\frac{\lambda \mathrm{z}}{\pi \mathrm{w_0^2}}\right)}, \tag{3.3}$$

and

$$\mathrm{R(z)} = \mathrm{z}\left(1 + \frac{\pi \mathrm{w_0^2}}{\lambda \mathrm{z}}\right)^2, \tag{3.4}$$

where $\mathrm{w_0}$ is the radius at the beam waist and λ is the wavelength of the laser beam.

Gaussian beams diverge as they propagate through the atmosphere [12]. The angle of divergence is given by [13],

$$\theta = \frac{\mathrm{w(z)}}{\mathrm{z}} \tag{3.5}$$

$$= \frac{\lambda}{\pi \mathrm{w_0}} \qquad \text{for } \mathrm{z} \gg \mathrm{Z}_R = \frac{\pi w_0^2}{\lambda}, \tag{3.6}$$

where Z_R is known as the Rayleigh range. To minimize the effect of beam divergence,

an optical device called a beam expander is used. It is designed to be an inverted telescope since a lens with a short focal length is placed in front of a lens with a longer length [13]. The lenses are separated by a distance equal to the sum of their focal lengths. This technique avoids large scale beam divergence, especially over long ranges such as in ranging and remote sensing.

References

[1] Wheeling Jesuit University n.d., *Layers of Earth's Atmosphere*, viewed 12 February 2014, from http://ete.cet.edu/gcc/?/volcanoes_layers/

[2] *Atmospheric Composition*, viewed 16 February 2014, from http://www.weather-climate.org.uk/03.php

[3] Andrews L. C. & Phillips, R. L., 2005. *Laser Beam Propagation Through Random Media*, SPIE Press, USA.

[4] Roddier F., 1981. "The effects of atmospheric turbulence in optical astronomy", *In: Progress in optics. Volume 19. Amsterdam, North-Holland Publishing Co. 1981, p. 281-376., 19,* 281-376.

[5] Ferraro P., Paturzo M. & Grilli S., 2007. "Optical Wavefront Measurement Using a Novel Phase-Shifting Point-Diffraction Interferometer", *SPIE Newsroom.*

[6] Medecki H., Tejnil E., Goldberg K. A., & Bokor J., 1996. "Phase-shifting point diffraction interferometer, *Optics Letters*, 21(19), 1526-1528.

[7] Kwon O. Y., 1984. "Multichannel phase-shifted interferometer", *Optics Letters*, 9(2), 59-61.

[8] Kadono H, Ogusu M. & Toyooka S., 1994. Phase shifting common path interferometer using a liquid-crystal phase modulator, *Opt. Commun.*, 110, 391-400.

[9] Mercer C. R., & Creath K, 1994. "Liquid crystal point-diffraction interferometer", *Optics Letters*, 19(12), 916-918.

[10] Chin S. L., 1989. *Fundamentals of Laser Optoelectronics*, World Scientific Publishing Co. Pte. Ltd., Singapore.

[11] Sasiela R. J., 1989. *Electromagnetic Wave Propagation in Turbulence*, 2nd Edition, SPIE, Washington.

[12] Webb H. R., 1996. "Confocal optical microscopy", *Reports on Progress in Physics*, 59(3), 427.

[13] Weichel H., 1990. *Laser Beam Propagation in the Atmosphere*, SPIE, USA.

Chapter 4

THEORY

4.1 The unperturbed and perturbed interference pattern

The distribution law for the intensity of light for an unperturbed interferogram is [1],

$$I(x,y) = 16\pi^2 A^2 a^4 \left(\frac{J_1(z)}{z}\right)^2 \cos^2\left(\frac{\pi^2 f_2 d}{\lambda F_2 D} x\right), \tag{4.1}$$

where,

- A is the constant amplitude of the plane laser beam wave,
- $2a$ is the diameter of each hole,
- d is the distance between the centres of the holes,
- D is the distance at which a plane is situated,
- $z = 2\pi\left(\frac{af_2\sqrt{x^2+y^2}}{\lambda f_2 D}\right)$,

- f_2 and F_2 are the focal distances of the objective lens l_2 and lens L_2 respectively,
- λ is the wavelength of the laser beam, and
- $J_1(z)$ is the Bessel function of 1st order.

The Bessell function $J_1(z)$ provides a series solution to second order differential equations [2]. Bessel functions in general are particularly useful for solving problems involving cylindrical symmetry [2]. Although useful, there are some difficulties present when working with Bessel functions. These include establishing whether a Bessel function can be applied to a systems equation and thereafter manipulating the systems boundary conditions. Much insight can be gained from numerous applications of Bessel functions some of which can be reviewed in [3]. The Bessel function can now be written as,

$$J_\nu(x) = \sum_{n=0}^{\infty} \left(\frac{(-1)^n}{\Gamma(n+1)\Gamma(n+\nu+1)} \right) \left(\frac{x}{2} \right)^{2n+\nu}, \tag{4.2}$$

and thereafter substituted into equation (4.3) to obtain the full expression for the perturbed interference pattern.

$I(x, y)$ describes the unperturbed intensity expression of the central diffraction spot region which provides the interference pattern [1, 4, 5]. The rate of diversion is determined by the beam radius (or spot size). Knowledge of the spot size is useful for determining how a beam expands or contracts over a path length. A small spot size diverges quicker and over short distances whereas a large spot size diverges slower

and over longer distances. Only the beam radius increases during propagation. Once turbulence has been introduced into the system, the laser beam experiences random directional fluctuations off the optical axis due to random changes in the refractive index of the atmosphere. There also exists amplitude and phase fluctuations in the laser beam wave front which induce intensity fluctuations of light waves by the process of diffraction [1, 4, 5]. This alters the light intensity curve in the interference pattern. The effect of fluctuating intensity is referred to as scintillation and will be discussed in more detail on page 57. The intensity expression $I_p(x, y)$ is presented in equation (4.3) for the perturbed interference pattern and can be obtained from the distribution law of light [1],

$$I_p(x, y) = I_{turb} \left(\frac{J_1(z)}{z} \right)^2 \cos^2 \left(\frac{\pi^2 f_2 d}{\lambda F_2 D} x - \frac{\psi}{2} \right), \tag{4.3}$$

where ψ is the phase difference between the light rays entering the slits.

4.2 Refractive index fluctuations

In the 1800's, Osborne Reynolds conducted experiments to better understand the turbulent nature of the atmosphere [6]. He described the atmosphere as having two distinct states of motion, namely laminar and turbulent. In laminar flow of a fluid, mixing does not occur since the flow is smooth, orderly and particles move with a constant velocity. In turbulent flow, the average velocity is higher and causes dynamic mixing which leads to random subflows known as turbulent eddies. To distinguish between laminar and turbulent flow, Reynold's numerous experiments yielded the

expression [7],

$$\mathrm{Re} = \frac{Vl}{\nu} \tag{4.4}$$

where, Re is the Reynolds number which is dimensionless, V is the mean velocity, ν is the kinematic viscosity of the fluid and l is the dimension of the flow. A value of $\mathrm{Re} < 2000$ describes a laminar flow while $\mathrm{Re} > 4000$ describes a turbulent flow. The region $2000 < \mathrm{Re} < 4000$ is known as transitional flow and is a region of medium velocity [7]. Close to the surface of the earth, approximate values of V, ν and l are $1\mathrm{ms}^{-1}$, $15 \times 10^{-6}\mathrm{m}^2\mathrm{s}^{-1}$ and 2 m respectfully. These values yield a Reynolds number of $\mathrm{Re} \approx 10^5$. In such a case, the atmosphere in general is regarded as highly turbulent.

A flow can also be characterised by measuring the variation of velocity at a random point within the flow [8]. Under turbulent conditions, the velocity at a point within the flow varies from the mean velocity. The degree of variation describes the turbulent intensity and is given by [8],

$$I = \frac{\sigma V_0}{V} \tag{4.5}$$

$$= \frac{V'}{V} \tag{4.6}$$

where σ is the standard deviation of the velocity of the flow, V_0 is the instantaneous velocity, V is the mean velocity and V' is the root mean square velocity.

4.3 Rytov theory

Optical turbulence effects such as scintillation, beam wander, scatter and intensity fluctuations are but a few effects which affect laser beam propagation in a turbulent environment. To describe weak irradiance fluctuations, the Rytov approximation is used. This yields all the statistical parameters using relatively simple mathematical expressions for the wave field [9]. The Rytov variance is the scintillation index which is calculated for a plane wave propagating in weak fluctuations and is used as a measure of optical turbulence strength. By definition, the Rytov variance is [10],

$$\sigma_R^2 = 1.23\, C_n^2\, k^{\frac{7}{6}}\, L^{\frac{11}{6}}, \tag{4.7}$$

where,

- σ_R^2 is the Rytov variance,
- C_n^2 is the refractive index structure parameter,
- λ is the wavelength,
- $k = \dfrac{2\pi}{\lambda}$ is the wave number, and
- L is the length which the beam propagates.

Classification of the Rytov variance [9],

$$\sigma_R^2 = \begin{cases} \ll 1 & \text{weak fluctuations} \\ \cong 1 & \text{moderate fluctuations} \\ \gg 1 & \text{strong fluctuations - saturation regime} \end{cases}$$

These classifications are however inadequate for a Gaussian-beam wave. The conditions which correspond to Gaussian-beam waves for weak fluctuations are given by [9],

$$\sigma_R^2 < 1 \qquad \text{and} \qquad \sigma_R^2 \Lambda^{\frac{5}{6}} < 1,$$

where,

- $\Lambda = \dfrac{2L}{kW^2}$, and

- W is the free space beam radius at the receiver.

Moderate to strong fluctuations exist if neither of the above conditions co-exist. For short propagation distances, as achieved in the laboratory, we assume spherical wave propagation. The scintillation index (σ_I^2) for a spherical wave is given by [9],

$$\sigma_I^2(\mathbf{r}, L) = 2.6056\, C_n^2\, k^2\, L^2 \int_0^1 \int_0^\infty \kappa \frac{\exp\left[\frac{-\kappa^2}{\kappa_m^2}\right]}{(\kappa^2 + \kappa_0^2)^{11/6}} \left(1 - \cos\left[\frac{L\kappa^2}{k}\xi(1-\xi)\right]\right) d\kappa\, d\xi \tag{4.8}$$

It has been shown by Andrews and Phillips [9] that equation (4.8) can be simplified to use results which are relatively easier to determine in a laboratory by,

$$\sigma_{I,l}^2(\mathbf{r}, L) = 2.6056\, C_n^2\, k^2\, L \times 0.188 \left(\frac{L}{k}\right)^{5/6} = 0.4\, \sigma_1^2 \tag{4.9}$$

which essentially describes a plane wave with a constant multiplier.

4.4 Kolmogorov theory of turbulence

The most common model used for describing turbulence in the atmosphere is the Kolmogorov model [11]. Kolmogorov imposed a few conditions for his theory, namely that the medium is incompressible and that the applied turbulence is homogeneous and isotropic. In spite of other useful models such as the von K*árm*á*n* model, the Kolmogorov model fairs well at both high and low frequencies [12]. Within the Kolmogorov spectrum, the refractive index fluctuations are valid over the inertial sub-range $L_0 \ll \kappa \ll l_0$ but can be extended over a wide range of wave numbers by making the assumptions,

$$l_0 \to 0 \qquad \text{and} \qquad L_0 \to \infty \tag{4.10}$$

In the real world however, these conditions are not meticulously satisfied. For regions outside of the inertial subrange, Kolmogorov's theory does not hold. When L_0 and l_0 influences are considered, the von K*árm*á*n* model can be used and is defined by [8],

$$\Phi_n(\kappa) = 0.033\, C_n^2\, \frac{\exp(-\kappa^2/\kappa_m^2)}{(\kappa^2 + \kappa_0^2)^{11/6}} \qquad 0 \leq \kappa < \infty \tag{4.11}$$

where $\kappa_0 = \dfrac{2\pi}{L_0}$ and $\kappa_m = \dfrac{5.92}{l_0}$. These redefined parameters allow deviations at the inner and outer scales and is shown graphically in Figure (4.1).

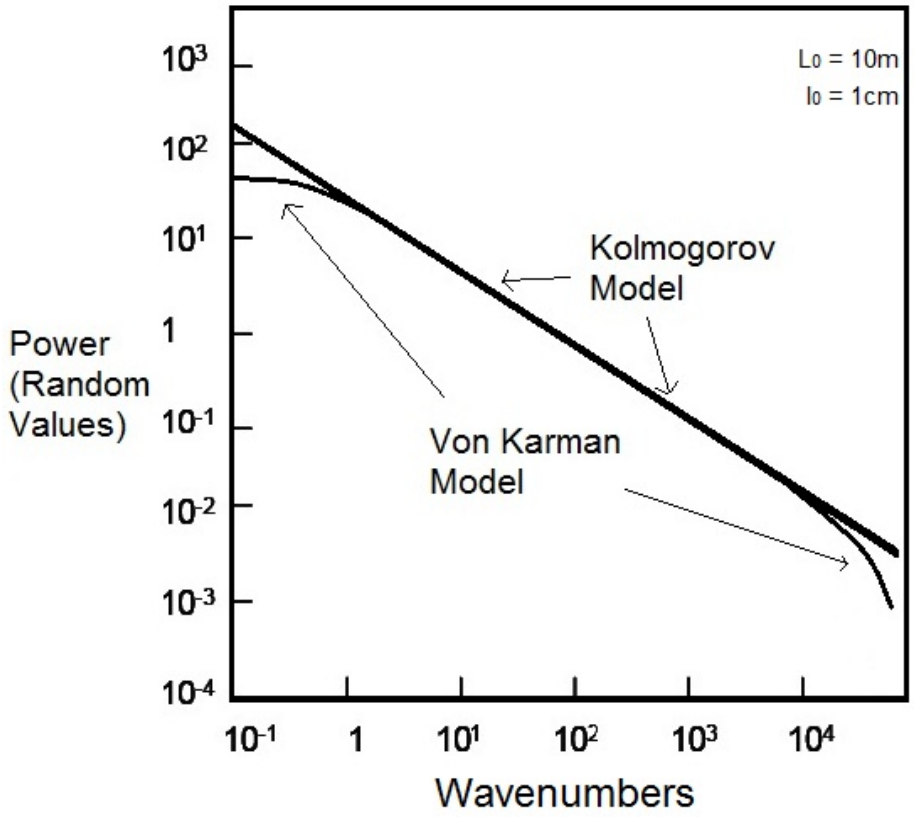

Figure 4.1: Comparison between Kolmogorov and von Kármán power spectral densities.

To better understand the structure of the atmosphere, Kolmogorov used a tool developed by Richardson, called *energy cascade theory* [13]. As mentioned previously, turbulent eddies in fluids arise due to random subflows caused by high average velocity fluctuations in the turbulent flow. In the atmosphere, the largest turbulent eddies are caused by factors such as wind shear and is known as the outer scale L_0. The dissipation of energy from the macroscale L_0 leads to a microscale l_0. The region between L_0 and l_0 is known as the *inertial range* and within these boundaries, Kolmogorov describes the kinetic energy as [13],

$$E(\kappa) = \sqrt{(\kappa_x^2 + \kappa_y^2 + \kappa_z^2)} \tag{4.12}$$

where κ represents the spatial wave number. Alternatively, by dimensional proportionality [13],

$$E(\kappa) \propto \kappa^{-\frac{5}{3}} \qquad \text{in the domain} \qquad \frac{2\pi}{L_0} \leq \kappa \ll \frac{2\pi}{l_0} \tag{4.13}$$

Depicted in Figure (4.2) is a description of turbulent eddies,

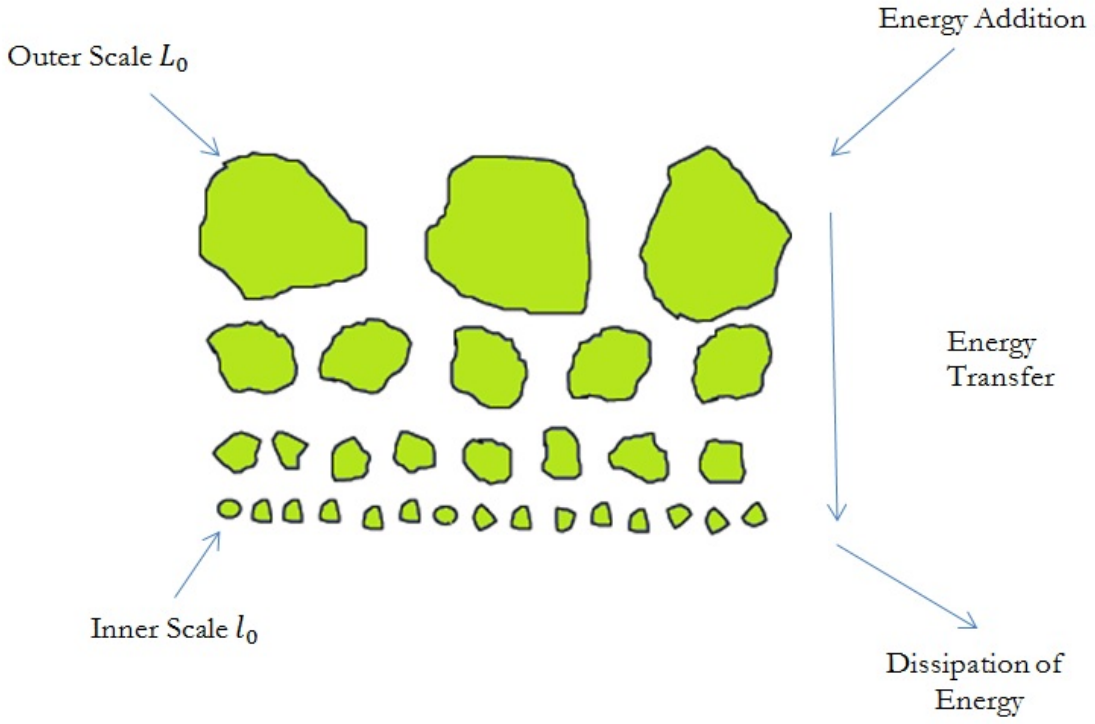

Figure 4.2: Diagrammatic depiction of turbulent eddies

The large eddies contain the bulk of the energy and are unstable. They break up into smaller eddies by releasing energy. This process is repeated until the Reynolds number is sufficiently small so that the turbulent eddies become stable.

For the case of temperature fluctuations, the region between L_0 and l_0 is known as the inertial convective range and represents the collection of eddies constrained

between L_0 and l_0.

4.5 Temperature structure function

Kolomogorov described the temperature fluctuations in terms of the refractive index structure according to Andrews and Phillips [13],

$$D_T(R) = \left\langle (T_1 - T_2)^2 \right\rangle = \begin{cases} C_T^2 l_0^{-4/3} R^{2/3}, & 0 \leq R \ll l_0 \\ C_T^2 R^2, & l_0 \ll R \ll L_0 \end{cases}$$

where T_1, T_2 are the temperatures at two points separated by a distance R and C_T^2 is the temperature structure constant. The inner scale l_0 is related to the average energy dissipation rate ϵ by [13],

$$l_0 = 5.80 \left(\frac{D^3}{\epsilon} \right)^{1/4}, \tag{4.14}$$

where D is the diffusivity of heat in air. The temperature fluctuations are in essence the key factor which affects optical wave propagation since the refractive index of the atmosphere varies according to the smallest scale temperature increment. At any point in space $\mathbf{R}$, the refractive index is expressed as [13],

$$n(\mathbf{R}) = 1 + n_1(\mathbf{R}), \tag{4.15}$$

where $n(\mathbf{R})$ has been normalised by its mean value n_0. In addition, fluctuations in the refractive index can be expressed in terms of temperature and pressure by [13,14],

$$n(\mathbf{R}) = 1 + 77.6 \times 10^{-6}(1 + 7.52 \times 10^{-3}\lambda^{-2})\frac{P(\mathbf{R})}{T(\mathbf{R})} \tag{4.16}$$

$$\cong \left(1 + 79 \times 10^{-6}\right)\frac{P(\mathbf{R})}{T(\mathbf{R})}, \tag{4.17}$$

where λ is the wavelength in μm and is set to a typical value of $\lambda \approx 0.5\mu$m, P is the pressure in millibars and T is the temperature in kelvin.

4.6 Refractive-index structure function

The inertial subrange has the properties of being statistically homogeneous and isotropic. This leads to the determination of the structure function in terms of the index of refraction structure constant C_n^2, the inner scale l_0 and a point in space $\mathbf{R}$ as [13],

$$D_n(R) = 2\left[B_n(0) - B_n(R)\right] = \begin{cases} C_n^2 l_0^{-4/3} R^2, & 0 \leq R \ll l_0 \\ C_n^2 R^{2/3}, & l_0 \ll R \ll L_0 \end{cases}$$

where B_n is the covariance function and the inner scale is [13],

$$l_0 = 7.40\left(\frac{\nu^3}{\epsilon}\right)^{1/4}, \tag{4.18}$$

where ν is the kinematic viscosity. The C_n^2 constant is a measure of the strength of the fluctuations in the refractive index [13]. The structure constant can be calculated

for a beam propagating in the atmosphere in terms of the temperature constant C_T^2 by [13, 14],

$$C_n^2 = \left(79 \times 10^{-}6\frac{P}{T^2}\right)^2 C_T^2. \tag{4.19}$$

Furthermore, the power spectrum of the refractive index fluctuations can be determined as [15],

$$\Psi_n(\kappa) = 0.033\, C_n^2 \kappa^{-\frac{11}{3}}. \tag{4.20}$$

4.7 Fourier transforms applied to image analysis

Spectral analysis can be used to express an image in its sine and cosine components. The image is represented in the spacial domain and is equivalently transformed into the frequency or fourier domain. A fast fourier transform (FFT) resolves an image into two components, namely its magnitude and phase. The magnitude is useful for image processing since all the frequencies which compose the image are specified. Making reference to Figure (4.3), the image is formed onto a 2D plane in polar representation and shows that the image contains various components and that their magnitudes decrease for larger frequencies. The central bright spot is known as the zero frequency zone or direct current zone and represents the average colour value of the entire image [16]. Additionally, the image does not contain imaginary components and thus the magnitude at the centre has a zero phase resulting in a gray spot.

The phase image is shown on the bottom right of Figure (4.3). Each pixel in

the image is given a value which determines the phase of the corresponding frequency. Due to the phase images not providing sufficient new information to describe the image any further, we will restrict ourselves to the frequency domain. For a square image of size N×N, the two-dimensional FFT is [17],

$$F(k,l) = \sum_{i=0}^{N-1} \sum_{j=0}^{N-1} f(i,j) \exp\left(-i\,2\pi\left(\frac{k\,i}{N} + \frac{l\,j}{N}\right)\right), \tag{4.21}$$

where,

- $f(i,j)$ is the phase image, i.e. spatial domain,
- the exponential term represents the basis function which correlates to each point given by $F(k,l)$.

Equation (4.22) can be summarised as follows; each point $F(k,l)$ is calculated by multiplying the spatial image with the base function and summing over the result.

Presented in Figure (4.3) is an unperturbed interferogram which has been subjected to a FFT. The result is two images represented in the frequency and spatial domains.

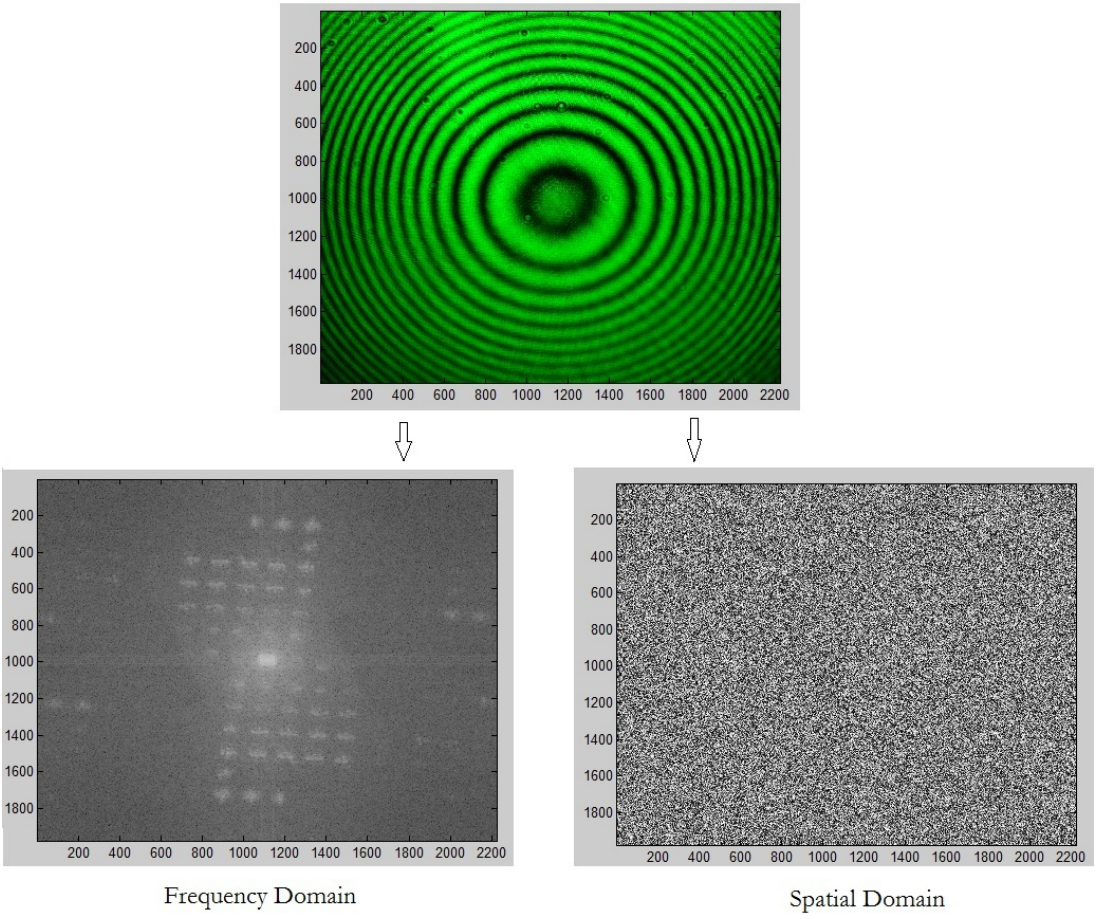

Figure 4.3: The unperturbed interferogram represented in the frequency and spatial domains using a FFT

Resolving the Fourier image back to the spatial domain can be achieved by applying the inverse Fourier transform given by [17],

$$f(a,b) = \frac{1}{N^2} \sum_{k=0}^{N-1} \sum_{l=0}^{N-1} F(k,l) \exp\left(-i\,2\pi \left(\frac{k\,a}{N} + \frac{l\,b}{N}\right)\right), \tag{4.22}$$

where the $\frac{1}{N^2}$ term represents the normalisation term.

References

[1] Hona J., Nyobe E. N. and Pemha E., 2008. "Experimental Technique Using an Interference Pattern for Measuring Directional Fluctuations of a Laser Beam Created By a Strong Thermal Turbulence", *Progress In Electromagnetic Research*, 84, 289-306.

[2] Niedziela J., 2008. Bessel Functions and Their Applications. Univ. of Tennessee Knoxville.

[3] Relton F.E., 1964. "Applied Bessel Functions", Blackie and Son Limited. *Experiments in Fluids*, 11-16.

[4] Pemha E. and Nyobe E. N., 2005. "Propagation of a Laser Beam Through a Plane and Free Turbulent Heated Air Flow: Determination of The Stochastic Characteristics of The Laser Beam Random Direction and Some Experimental Results", PIER, 53, 31-53.

[5] Pemha E. and Nyobe E. N., 2011. "Genetic Algorithm Approach and Experimental Confirmation of a Laser-based Diagnostic Technique for the Local Thermal Turbulence in a Hot Wind Tunnel Jet", PIER B, 28, 325-350.

[6] Reynolds O., 1883. "An experimental investigation of the circumstances which determine the motion of water shall be direct or sinuous, and of the law of resistance in parallel channels," *Phil Trans Roy Soc*, 174, 935-982.

[7] Benson T., 2014. *Reynolds Number*, viewed 19 February 204, from https://www.grc.nasa.gov/www/k-12/airplane/reynolds.html

[8] Isterling W. M., 2010. *Electro-Optic Propagation Through Highly Aberrant Media*, Phd Thesis, University of Adelaide, Australia.

[9] Andrews L. C. & Phillips, R. L., 2005. *Laser Beam Propagation Through Random Media*, SPIE Press, USA.

[10] Thomas E. F., 2005. *The Scintillation Index in Moderate to Strong Turbulence for the Gaussian Beam Wave Along a Slant Path*, MSc thesis, University of Central Florida, USA.

[11] Kolmogorov A. N., 1991. "The Local Structure of Turbulence in an Incompressible Fluid for Very Large Reynolds Numbers", *Proceedings of the Royal Society of London. Series A: Mathematical and Physical Sciences, 434*(1890), 9-13.

[12] Consortini A. and O'Donnell K. A., 1993. "Measuring the inner scale of atmospheric turbulence by correlation of lateral displacements of thin parallel laser beams", *Waves in random media*, 3(2), 85-92.

[13] Andrews L. C. & Phillips, R. L., 2005. *Laser Beam Propagation Through Random Media*, SPIE Press, USA.

[14] Weichel H., 1990. *Laser Beam Propagation in the Atmosphere*, SPIE, USA.

[15] Tatarskii V. I., 1961. "Wave Propagation in a Turbulent Medium Translated From Russian by R. A. Silverman and McGraw-Hill", 134(3475), 324-345.

[16] Weinhaus F., 2011. *ImageMagick v6 Examples-Fourier Transforms*, viewed 23 February 2014, from http://www.imagemagick.org/Usage/fourier/

[17] Fisher R., Perkins S., Walker A. & Wolfart E., 2003. *Fourier Transform*, viewed 23 February 2014, from http://homepages.inf.ed.ac.uk/rbf/HIPR2/fourier.htm

APPENDIX A

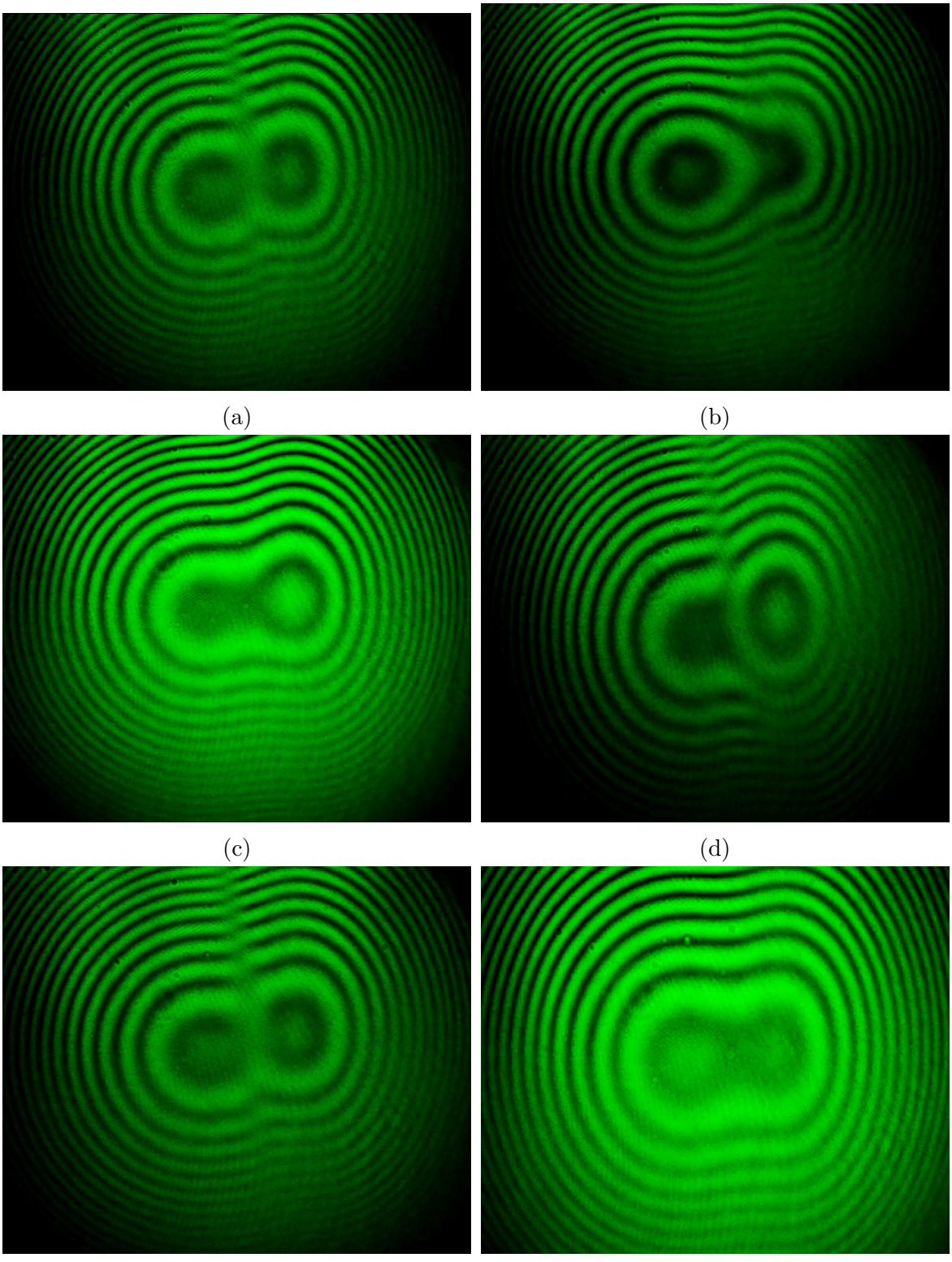

(a) (b)

(c) (d)

(e) (f)

Figure 4.4: Perturbed interferograms obtained using a lighter as a turbulence source

Part II

PUBLICATIONS

Paper 1

Chapter 1

EXPERIMENTAL VERIFICATION OF THE TURBULENT EFFECTS ON LASER BEAM PROPAGATION IN SPACE ⋆

⋆Augustine S. M. and N. Chetty, 2014. Experimental verification of the turbulent effects on laser beam propagation in space. *Atmósfera*, 27(4), in press.

Experimental Verification of the Turbulent Effects on Laser Beam Propagation in Space

S. M. Augustine and N. Chetty[1]

School of Chemistry and Physics, University of KwaZulu-Natal, Pietermaritzburg, South Africa, 3201

[1]*ChettyN3@ukzn.ac.za*

Abstract: In this work, we have modified an existing experimental setup to fully classify the thermal effects on a laser beam propagating in air. Improvements made to the setup include a new, more powerful laser, a precision designed turbulence delivery system, an imbedded pressure sensor, a platform for height adjustability between the laser beam and the turbulence model. The setup was not only able to reproduce previous results exactly but also allowed new data for the turbulence strength C_n^2, the Rytov variance (scintillation) and the coherence diameter (Fried's parameter) to be successfully measured. Analysis of the produced interferograms has been discussed using Fast Fourier Transforms. The results confirm, within the Kolmogorov regime, that phase and intensity fluctuations increase relative to temperature. The turbulent region exhibited very strong turbulence, in the range $1.1 \times 10^{-12}\,\mathrm{m}^{-2/3}$ to $2.7 \times 10^{-12}\,\mathrm{m}^{-2/3}$. In spite of the strong turbulence strength, the scintillation proved otherwise, since the condition for a weak turbulence environment was determined in the laboratory a low scintillation index is to be expected. This is as a result of the relatively short propagation distances achieved in the laboratory. In the open atmosphere, path lengths extend over vast distances and in order for turbulent effects to be realised, the turbulence model must generate stronger turbulence. The model was, therefore, able to demonstrate its ability to fully quantify and determine the thermal turbulence effects on a propagating laser beam.

1. Introduction

Theories relating to atmospheric turbulence have been studied over many decades in order to better understand the impact of turbulence on the propagation of a laser beam through the atmosphere (Tatarskii,1961). Turbulence can be described as the random mixing of air particles in the atmosphere due to either rapid or small scale spatial and temporal refractive index fluctuations in temperature (Shaik, 1988 and Ishimaru, 1981). Although slight variations in temperature can cause changes in the refractive index of air (of the order 0.1 K - 1.0 K), the accumulative effect of such inhomogeneities expanding over vast distances poses significant challenges for laser beam propagation (Baak, 1969 and Prod'homme, 1969). Research has shown that refractive index fluctuations of the atmosphere are significant near the surface of the Earth and negligible at higher altitudes (Andrews and Phillips, 1988). These refractive index fluctuations cause random phase perturbations of the laser beam which can lead to beam distortion (Chatterjee and Fathi, 2014). In addition, laser propagation through turbulent media can result in scintillation (Federico, 2004), beam wander (Berman *et al*, 2013) and beam spreading (Weichel, 1990). The extent to which these factors affect the beam depend largely on the varying nature of the turbulent eddies which exist at various altitudes. Knowledge of the effects, attained over the years, has been made use of notably in the domains of military (Titterton, 2005), radar (Mead, 1990), remote sensing (Shin, 1989), satellite communications (Ojo *et al*, 2008) and medical diagnostics (Lonappen, 2007 and Ibrahim, 2007). This paper presents new modifications to a model used by (Ndlovu, 2013) as it has proven to be robust, cost efficient and stable in detecting and fully quantifying the effects of thermal turbulence on laser beam

propagation in air. The previous method used a cigarette lighter as a turbulence source but this led to non-uniform heat distribution over a very small area (Ndlovu, 2013). We have, thus, in this work employed an automated heating plate for the turbulence re-creation. The design of the turbulence generator incorporates an aluminium panel with multiple high powered resistors arranged on the underside to provide consistent heating above. In addition, a pressure sensor was positioned within the turbulent region to determine any phase fluctuations resulting from a change in pressure. The high sensitivity of the device allowed slight variations in pressure change to be detected between the turbulent and non turbulent regions. The primary light source used in this work was a green continuous wave He-Ne 532 nm laser. To determine the effect of thermal turbulence on laser beam propagation, a complete analysis of the produced interferograms at various temperatures has been discussed using image analysis software. Furthermore, the turbulence strength C_n^2, the Rytov variance (scintillation) and the coherence diameter (Fried's parameter) have been determined in the laboratory and shown to coincide well with published values.

2. Theory

Random fluctuations in the refractive index of the atmosphere alter the propagation pathway of light beams which, in turn, effects their initial phase fronts. Once light propagates through a turbulent atmosphere, the phase fronts become distorted and experience random changes in beam direction (beam wander) as well as random intensity fluctuations (scintillation) (Berman *et al*, 2013). Scintillation can be classified as the fluctuations experienced in the received irradiance when light beams propagate through a turbulent atmosphere (Churnside

and Lataitis, 1990). Measuring certain observations in the laboratory allows the scintillation to be calculated from (Andrews and Phillips, 1988),

$$\sigma_R^2 = 1.23 C_n^2 k^{\frac{7}{6}} L^{\frac{11}{6}}, \tag{1}$$

where C_n^2 is the refractive index structure coefficient, k is the wavenumber and L is the propagation path length. The wavelength and path length are measured in the laboratory and C_n^2 is thereafter inferred.

Propagation of the beam through turbulent conditions has shown the beam to undergo a loss of coherence, focus and beam spread (Chernov, 1967 and Esposito, 1967). The extent to which scintillation and beam wander occur depends largely on the combination of temperature, wind velocity and convection factors (Titterton, 1973). The key to obtaining information about the way in which beams are affected by turbulence is to determine the refractive index structure coefficient C_n^2 given by (Andrews and Phillips, 1988),

$$C_n^2 = \left(79.0 \times 10^{-6} \left[\frac{\mathrm{p}}{\mathrm{T}^2}\right]\right) \mathrm{C}_T^2, \tag{2}$$

with

$$C_T^2 = \left(\sqrt{< (\mathrm{T}_1 - \mathrm{T}_2)^2 >}\right) \mathrm{r}^{-1/3}. \tag{3}$$

where p is the atmospheric pressure in millibars and $<>$ represents the ensemble average. C_T^2 is a measurable quantity defined by the temperature differences, T_1 and T_2, between two reference points separated by a distance r. C_n^2 is a parameter which changes as a function of altitude and alters the behaviour of the aberrations. The following characterises the optical energy of and measures the

atmospheric turbulence contributions for a wave that propagates through it. As C_n^2 increases, so does the effect of the aberration. Typically, C_n^2 decreases in relation to the altitude (Andrews and Phillips, 1988). The refractive index structure coefficient alone provides adequate information about the turbulent region and typically ranges from $10^{-17}\mathrm{m}^{-2/3}$ or less for weak turbulences and $10^{-13}\mathrm{m}^{-2/3}$ or more for strong turbulence (Andrews and Phillips, 1988 and Weichel, 1990).

Advances made by (Strohbehm, 1978) have shown methods of determining the phase structure function D_s, beam size W and the coherent intensity of the beam. These expressions are useful for modelling the intensity of the laser beam propagating through an inhomogeneous medium and incident on a distant target. As the laser beam propagates through turbulent media, there is a redistribution of its intensity which may be determined according to (Strohbehm, 1978), as

$$I(\rho_c, z) = A_0^2 \frac{2W_0^2}{W^2} \exp(-\alpha_E z) \int_0^\infty t\, J_0(t\,\rho') \times \exp\left[-t^2 - \left(\frac{1}{2}\right) D_s t^{5/3}\right] \mathrm{d}t, \quad (4)$$

where, A_0 is the uniform amplitude of the plane laser wave, W_0 the Gaussian beam size, J_0 the first-order Bessel function, ρ is the transverse distance from the beam, W the beam size at z and where z lies within the domain,

$$(0.39 C_n^2 k^2 l_0^{5/3})^{-1} \gg z \gg (0.39 C_n^2 k^2 L_0^{5/3})^{-1}, \quad (5)$$

Particular emphasis is placed on the phase structure function as it represents a measure of the correlation of the phase between two points in a plane traversing perpendicularly to the direction of propagation. The phase structure function D_s and atmospheric coherence diameter r_0 are given by (Strohbehm, 1978) and

(Magee, 1993),

$$D_s = 2.91 C_n^2 r^{5/3} z \left(1 - 0.8 \left(\frac{2\pi r}{L_0}\right)^{1/3}\right), \tag{6}$$

and

$$r_0 = 0.185 \left[\frac{\bar{\lambda}^2}{\int_0^z C_n^2(\xi)\, d\xi}\right]^{3/5}, \tag{7}$$

with r being the separation between the inner and outer scales, z the propagation path length, and $\bar{\lambda}$ the wavelength of the laser beam. The coherence diameter is a measure of the quality of the optical signal through the atmosphere (Magee, 1993). Typical values of r_0 at a good observatory range between 5 cm to 20 cm and depends largely on the seeing conditions. The highly stochastic nature of the atmosphere determines the seeing strength (Magee, 1993). At high altitude, turbulent effects are relatively weak, resulting in optical imaging effects being unaffected. Such conditions infer good seeing conditions. Closer to the ground however, seeing conditions worsen and can be attributed to weather conditions, as well as the highly turbulent atmosphere.

3. Description of the components

We consider a laser beam propagating through an inhomogeneous medium. The laser beam propagates through the following optical components, a microscope objective lens, the turbulence model and pressure sensor, a series of collimating lenses, a spatial filter, a point-diffraction interferometer and falls incident on a camera. The camera acts as a detector to take photographs of the interferograms and display the interference pattern on a monitor. The entire setup is mounted on height adjustable rails to vary the separation between the laser beam and

turbulence generator. The lowest height setting has been used in this work, corresponding to a separation of 28 mm between laser beam and turbulence source. Presented below in Figure 1 is a schematic diagram of the apparatus showing the complete optical train.

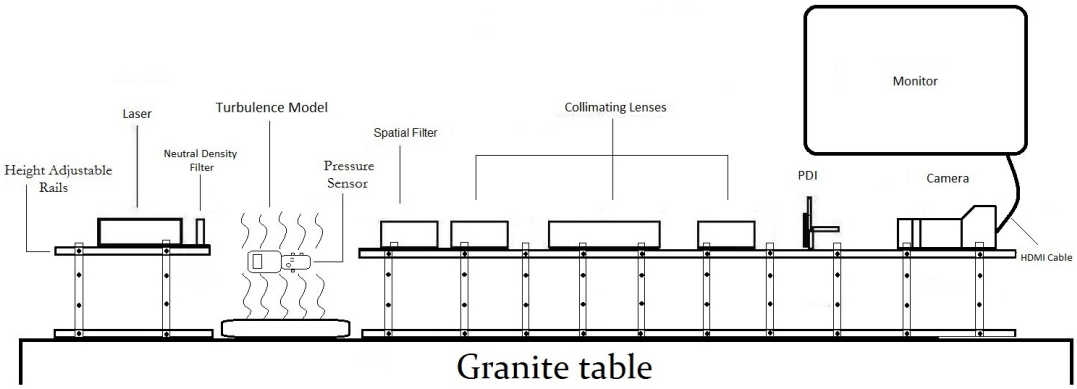

Fig. 1. 2D side view of complete optical train with height adjustable rails.

3.1. The laboratory, granite table and optical bench

The experiment was assembled on a granite table top with dimensions 1.2 m by 2.5 m. The granite table presented a stable platform which protected the components from bumps and knocks as well as internal and external vibrations caused by the local environment. The experiment took place in a dark room 5 m by 5 m and was structurally closed off from the outside environment as there were no windows or ventilation outlets.

3.2. The dovetail rail

An Edmund dovetail v-block rail (Model no. 54-402) of length 91.44 cm was used for the main receiver train. The rail was divided into three sections to allow better alignment of the optical components and, more importantly, to provide

space for the inclusion of the turbulence model. A 60.96 cm rail was used to hold the collimating lenses and two 15.24 cm sections, one for the light source assembly and the other for the camera assembly. All the rails were supported by and screwed down onto five (150 mm by 150 mm) bench plates manufactured by Edmund (Model no. 53936). These bench plates had a 13 mm thickness. Each bench plate was drilled with M6 holes arrayed on a pitch of 25 mm. This helped in aligning the optical components with the light source.

3.3. The light source and neutral density filter

A 29.4 mW laser of wavelength 532 nm was mounted in conjunction with a microscope objective and collimating lens of 160 mm focal length. The microscope objective reduces the beam diameter to 1/20 of its original size. The collimating lens adjusts the beam diameter to 25 mm. The light source assembly consisted of a laser diode, a plastic aspheric collimator and holographic diffuser. The plastic collimator and the holographic diffuser were mounted in separate 25 mm T-mount cells. The light source assembly was mounted on a micro-optical bench which was glued onto a 6" dovetail rail to avoid movements and vibrations from the surroundings. A reflective neutral density filter 3.0 optical density 50 mm by 50 mm with 1.5 mm thickness manufactured by Edmund optics (Model no. 46-126) was placed just in front of the light source. This reflective filter helped in reducing the laser beam intensity and eliminated stray-light artifacts so that clear and bright interferograms were produced for analysis. The automated turbulence model was introduced within a 200 mm gap between the light source assembly and the main receiver train.

3.4. The collimators

Three collimating lenses of 200 mm focal length were housed by collimator holders, 121.5 mm long and placed on a 60.96 cm dovetail rail. The collimating lenses were moved back and forth such that the laser beam was focused, and this also served the purpose of reducing the effects of beam wander and beam spreading. The focus was adjusted by noting the size of the beam formed on the PDI plate. A focused beam is necessary as the PDI plate presents on its surface a point discontinuity in the form of a pinhole through which the laser beam enters.

3.5. The point-diffraction interferometer

The point diffraction interferometer (PDI) manufactured by Astro Electronics was used in this work. It consisted of 55 pinholes which were distributed on an array of pitch 1 mm. The PDI was mounted, together with the carrier cell, on an Edmund XYZ stage. There were three adjustments on the XYZ stage that were used to locate the laser beam so that it could pass through the PDI pinhole. The PDI was mounted between the third collimator and the camera assembly so that the beam would pass through the pinhole and form interferograms that would be detected by the camera.

3.6. The camera

While it may be necessary to use a monochrome video camera which has a substantial frame-rate, a much more feasible alternative is to use an ordinary Digital Single Lens Reflex (DSLR) camera such as the Nikon D3100. The DSLR camera features a Live View mode with a very high resolution which was necessary

for this work. An external power supply was added since the Nikon batteries run down fairly quickly. The camera was mounted on a 15.24 cm dovetail rail and held down by a strap-down bar. The camera was modified to accommodate an Edmund lens holder which, in turn, housed a double lens of focal length 150 mm.

3.7. The display monitor

A Samsung 23 inch high definition (HD) monitor was used to display the live video feed since it allowed a direct HD connection from the Nikon D3100. An HD monitor is necessary since the displays are crisp and allow easier visual inspection of the produced interferograms.

3.8. The height adjustable rails

The design incorporated two aluminum sheets, 1 cm thick with lengths of 30 cm and 170 cm. Along either side of the sheets, vertical strut bars were welded, each having a height of 32 cm. Holes were drilled along the height of the bars, spaced at 5 cm intervals. The aluminium sheets were also tapped with threads, allowing the optical components to be fastened down. The manufacture of the design was precision engineered by the mechanical instrument workshop (MIW). Initial experimental runs were conducted at the lowest setting which corresponds to no height adjustment.

3.9. The turbulence model and thermocouple

Turbulence was created by a specially manufactured heated aluminum panel, 1 cm thick with dimensions 20 cm$\times$20 cm. Arranged on the underside of the panel was an array of high powered resistors which were fixed into position

using steel nuts and bolts. The electronics department carefully constructed the arrangement of the resistors such that consistent heating existed above the panel. This was achieved using a surface temperature probe to measure the temperature at different points on the panel and thereafter, placing appropriate resistors to accommodate their position. The aluminium panel was snugly placed in a case on a bed of fire blanket, which insulated it from external factors. The resistors varied in their resistances, according to Figure 3, with the corresponding power values represented in Figure 4. The temperature range was controlled between 0° and 180° Celsius using a proportional integral derivative (PID) controller. The device served the purpose of setting, monitoring and controlling the temperature of the panel. Temperature measurements were taken using a sensitive J-type thermocouple with two decimal precision. Table (2) shows the results obtained from the experiment for temperature versus the position from the centre of the panel, with the centre point represented by 0 cm. Negative values represent a position left of centre and positive values represent a position right of centre. The temperature of the PID was set to a value of 100° Celsius which corresponds to the temperature of the panel as determined using a surface temperature probe. Sufficient time was given for the air temperature to stabilise before readings were taken.

Position from centre of panel(cm)	Air temperature(°C)
(Left of centre -20)	40.55
-15	40.47
-10	40.53
-5	40.26
(Centre of panel)	40.34
5	40.39
10	40.46
15	40.51
(Right of centre 20)	40.37

Table 1. Relationship between the position from the centre of the heated panel and air temperature

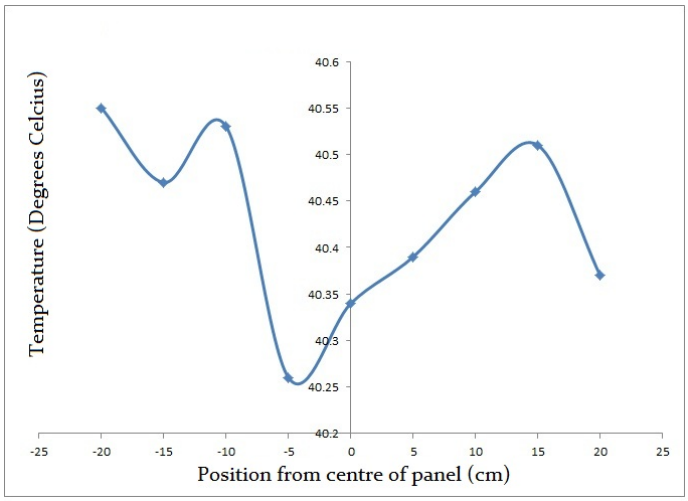

Fig. 2. Temperature of turbulence model plate at various positions.

Clearly from Figure 2, the heated panel is successful in maintaining a uniform heat distribution along the surface of the panel with a standard deviation of 9.7×10^{-2}°C. The turbulence generated by the model was, therefore, effective in modelling an inhomogeneous and isotropic environment within an area of 0.04 m^2. The following Figures 3 and 4 explicitly show the arrangement of the resistors on the panel. Figure 3 presents the resistance values of the resistors in

ohms(Ω).

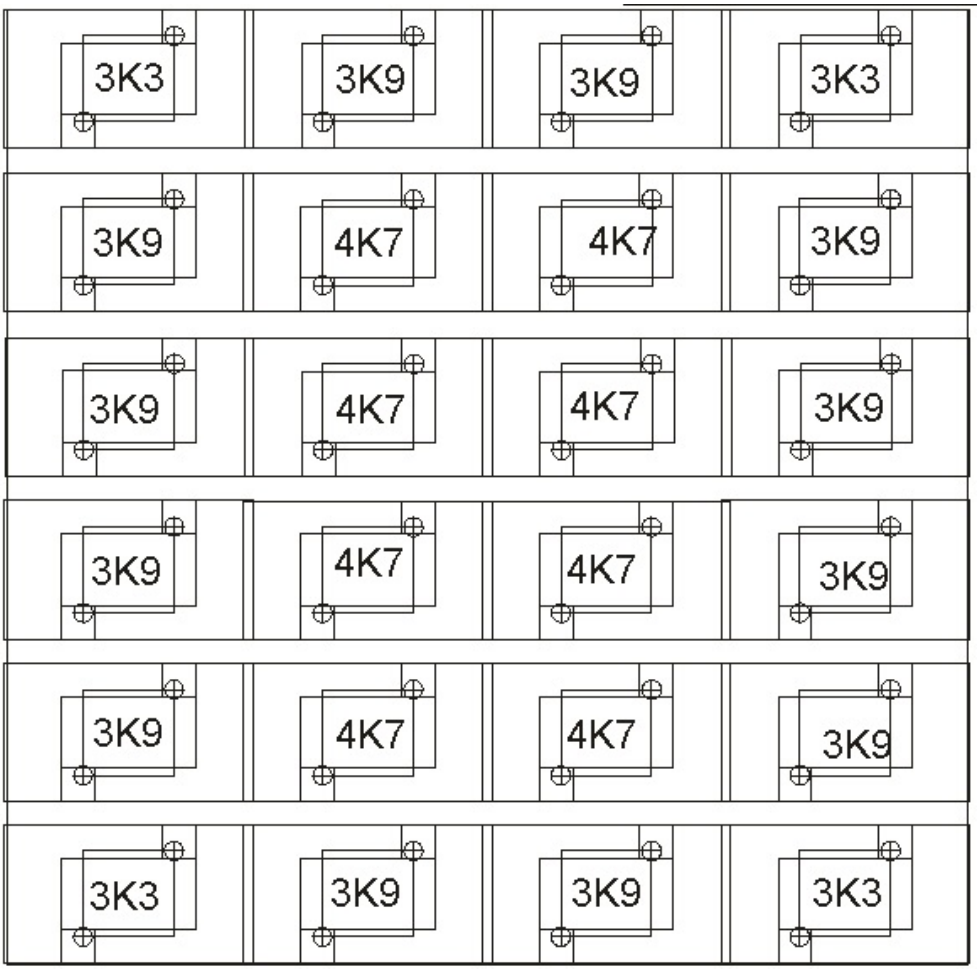

Fig. 3. Schematic resistance diagram of turbulence panel.

The resistances shown in Figure 3 are written in standard form where 3K3≡3300Ω, etc. So naturally, according to $P = \frac{V^2}{R}$, a smaller resistance corresponds to a larger power.

Figure 4 presents the power values associated with the resistors in watts (W).

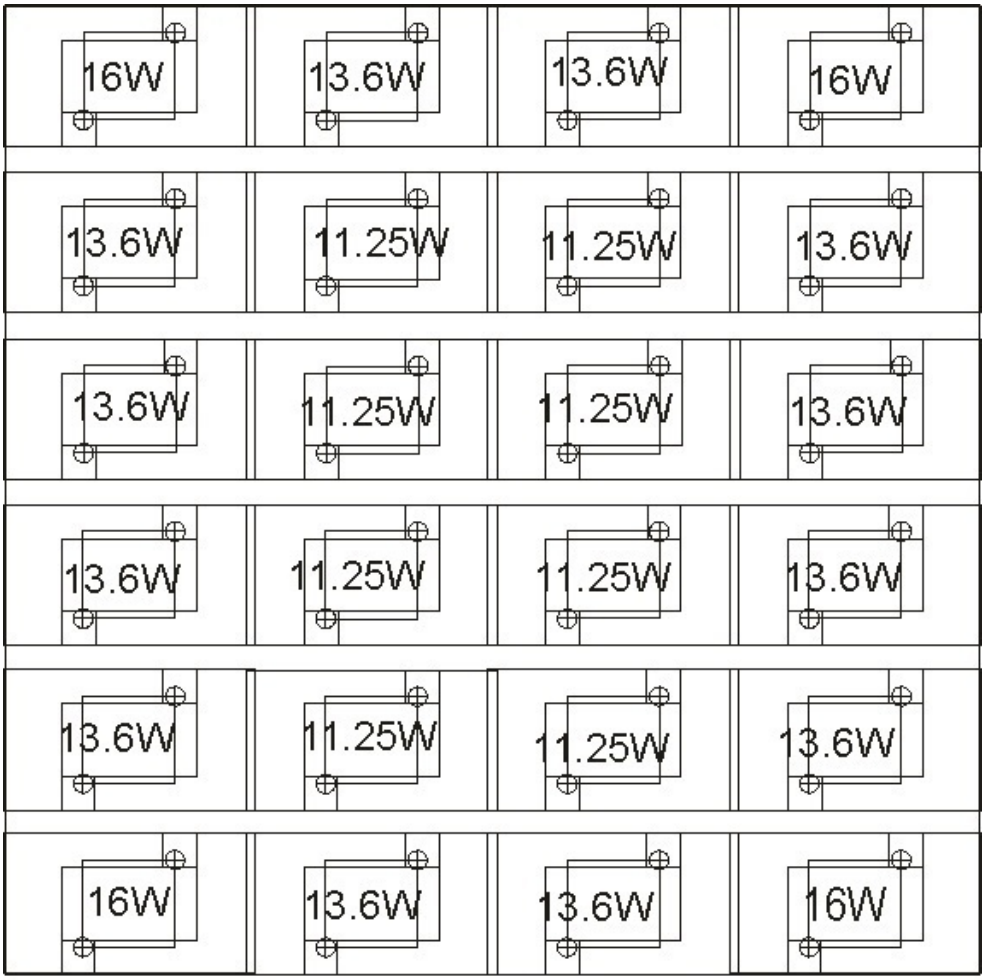

Fig. 4. Schematic power diagram of turbulence panel.

Intuitively, the largest powered resistors are on the corners since they are exposed on 2 of their 4 sides to natural elements. Thus, more power is needed to maintain the heat on the corners as opposed to the centre of the panel namely 29.7% more power.

4. Experimental Procedure

4.1. Layout

A schematic layout of the design with the turbulence model included is presented in Figure 5.

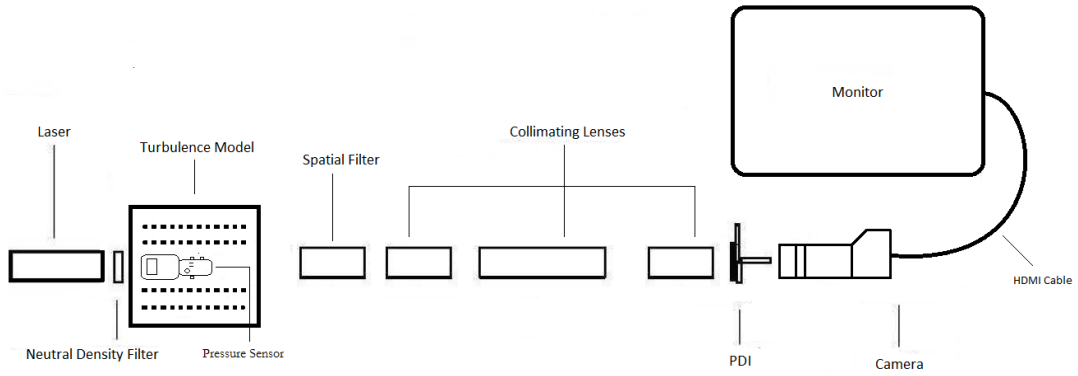

Fig. 5. 2D top view of the complete optical train.

As described in Section 3.2, the Edmund optics rail was divided into 3 sections. The laser was mounted on the first 15.24 cm rail. The longer 60.96 cm rail supported the 3 collimators and PDI. The last 15.24 cm rail supported the camera.

A crucial step in the setup of the apparatus was to reduce dust in and around the laboratory. Minimal levels of dust are extremely detrimental to the produced interferograms as light is scattered by the dust particles leading to stray light artifacts falling upon the detectors. This in turn causes inconsistent intensity profiles which are uncharacterisable. To ensure that the optical components are free from dust, Dust off and methanol were periodically used to clean the surfaces of the optical lenses with lens tissue. In addition, the apparatus were always covered when not in use.

4.2. Description

The turbulence model was used to generate a uniformly heated panel which could be varied by the user. The heat emanating from the panel randomly influences the refractive index of air which results in random fluctuations of the phase fronts of the laser beam. A wide range of temperatures could be tested as the model used a sophisticated PID algorithm control unit. Further measures were taken for precision purposes: a surface temperature probe was used to verify the temperature of the air just above the panel.

Further modification of the turbulence model involved the inclusion of a pressure sensor which monitored the pressure in and out of the turbulent region. The differential of pressures existing between the regions was measured on the devices most sensitive setting, i.e., 0-100 Pa.

A reflective 50 mm by 50 mm 2.5 OD neutral density filter of 2.0 mm thickness was positioned immediately after the laser as it served the purpose of reducing any stray light in the produced interferograms. Some filters considerably reduced the intensity of the light falling upon the PDI hence numerous tests were conducted to determine the most effective filter whilst ensuring bright, clear and characterisable interferograms. Presented in Figure 6, is an examples of an interferogram, one of which does not have a ND filter (on the left) while the other does (on the right). The left interferogram of Figure 6 has in it random light artifacts which are not filtered out by the spatial filter and collimators. The right interferogram of Figure 6 used the above mentioned ND filter to produce a flawless image, clearly depicting a Gaussian form profile

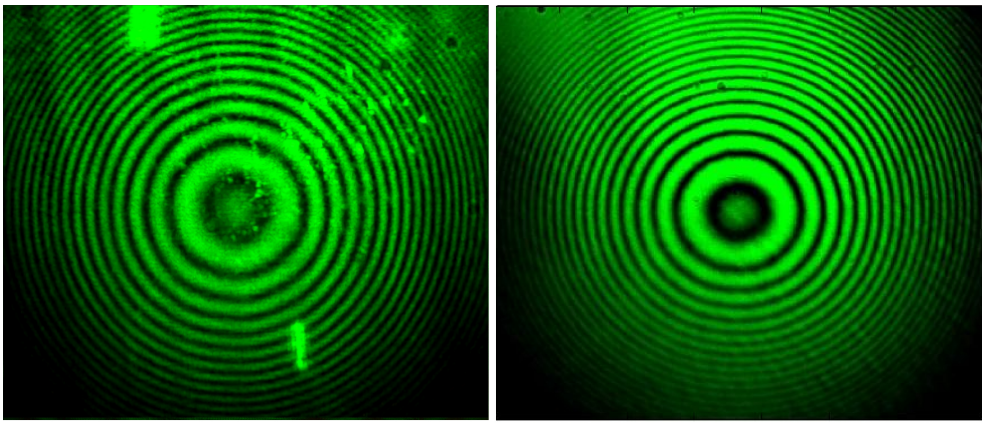

Fig. 6. Comparison of a non present ND filter with a present ND filter.

for an unperturbed laser beam. A more descriptive discussion of the profile is provided in the results section. With the correct ND filter chosen and in place, the proceeding collimators were moved back and forth to yield a focused beam at the PDI pinhole. By doing so, a Gaussian form intensity profile was produced which provided stable and clear interferograms. At all times, alignment was perilous and utmost care was taken in ensuring a centralised beam. The final component in the optical train was the DSRL camera and it was positioned to receive the laser beam at the centre of its aperture.

An HDMI cable transferred the captured image onto a 23 inch HD screen. Interferograms were then used to study the effect of thermal turbulence on a propagating laser beam. This was done by extracting the wavefront information using the phase shifts that formed on the interferograms due to thermal perturbations on the propagating laser beam. The wavefronts were analysed using ImageJ and Matlab. A description of the findings will be discussed later.

5. Results, analysis and discussion

Data analysis began at a room temperature of 23.1°C. The temperature of the air was measured using a thermocouple which was positioned in very close proximity to the laser beam. The value of the air temperature did not however, correlate with the apparent temperature of the heated panel. This could be due to heat being transferred only through convection. The table below shows the temperature of the heated aluminum panel against the temperature of the air, 28 mm above the heated panel.

Reading	Temperature of air °C	Temperature of plate °C
1	23.1	0
2	35.0	97
3	45.0	122
4	55.0	150
5	65.0	178

Table 2. Comparison between actual air temperature and temperature of the heated panel

Numerous experiments were performed over a number of days and the consistency of the interferograms was analysed and results averaged. The results on the following pages are a reflection of the averaged data, split into five categories. Five interferograms are depicted on the proceeding pages. Reading 1, Figures 7-9, are the data for the unperturbed laser beam at a room temperature of 23.1°C. Readings 2 to 5 present the data for the perturbed laser beam, which was subjected to thermal turbulence of 35°C, 45°C, 55°C and 65°C.

5.1. *Reading 1 (At 23.1°C)*

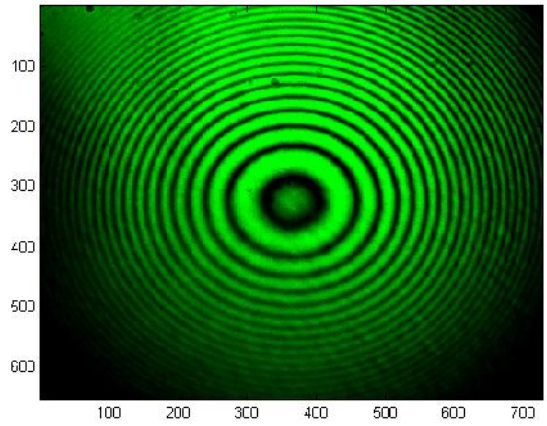

Fig. 7. Unperturbed interference pattern.

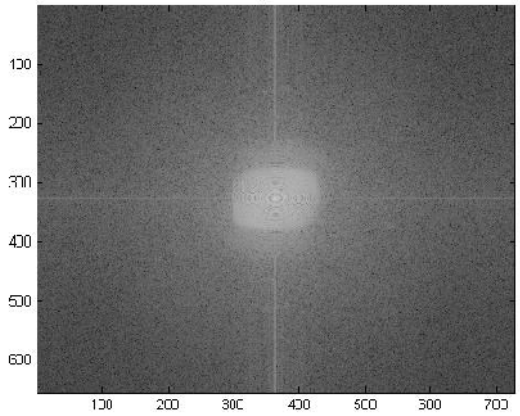

Fig. 8. The magnitude of the FFT.

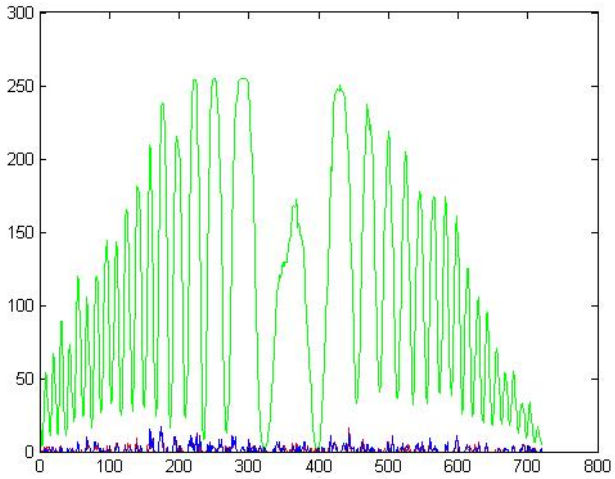

Fig. 9. Intensity profile of the unperturbed interferogram.

To determine the extent to which the thermal turbulence affected the propagating laser beam, it was necessary to compare readings 2 - 5 with reading 1. A Fast Fourier Transform (FFT) was used, since it resolves an image into its magnitude and phase domains. The magnitude is useful for image processing since all the frequencies which compose the image are specified. Due to the phase images not providing sufficient new information to describe the image any fur-

ther, we will restrict ourselves to the frequency domain. Making reference to Figure 8, the image is formed on a 2D plane in polar representation and shows that the image contains various components and that their magnitudes decrease for larger frequencies. The central bright spot is known as the zero frequency zone or direct current zone and represents the average colour value of the entire image. Additionally, the image does not contain imaginary components and, thus, the magnitude at the centre has a zero phase resulting in a grey spot. The large concentration around the centre point indicates a lower spatial frequency. Numerous adjustments can be made to the transformed image to either improve the focus or decrease blurriness and this can be achieved by applying a low pass filter to preserve the low frequency regions, or a high pass filter, to preserve the sharpness and defined edges. Intermittent filters can be applied and are known as band pass filters. For comparisons in subsequent readings we will compare their FFT's to Figure 8 by image subtraction. If the subtraction yields a completely grey image then it is implied that the two images coincide completely and, hence, there is no change in beam position or phase.

5.2. *Reading 2 (At 35.0°C)*

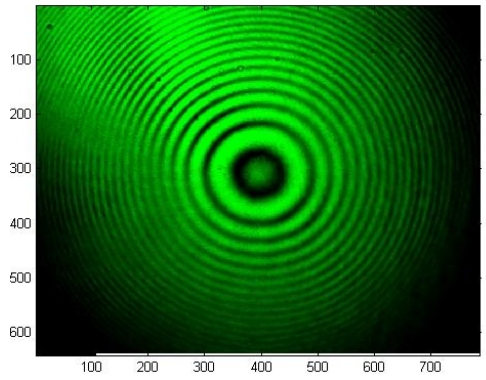

Fig. 10. Perturbed interference pattern.

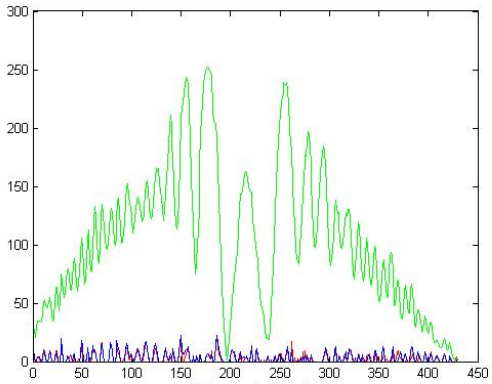

Fig. 12. Intensity profile at 35°C.

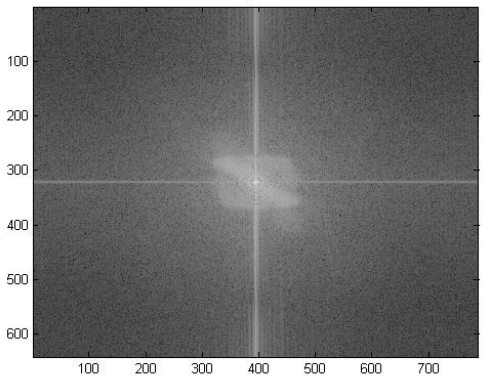

Fig. 11. The magnitude of the FFT.

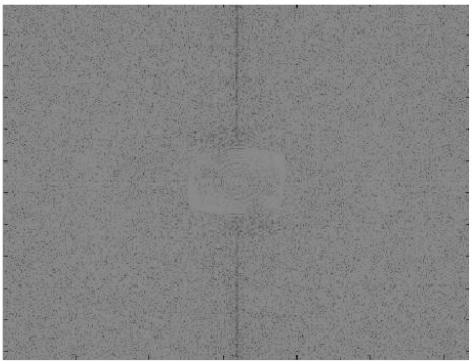

Fig. 13. Image subtraction of reading 2 from 1.

Reading 2 was taken at a measured air temperature of 35°C. Within the turbulent region, the laser beam is exposed to a temperature increase of 11.9°C above room temperature. The interferogram does not display signs of distortion or defocus but does have some signs of image blurring. The intensity distribution does imply some energy redistribution occurring between 50 and 150 units, as well as between 300 and 400 units. On analysis of Figure 13, the image subtraction describes an almost completely greyed out result, although there are black specs scattered randomly over the image. The large localisation around

the centroid of Figure 11 describes a larger lower spatial frequency distribution. The image subtraction data shows a vague outline of the centroid in black Figure 13. According to (Banish, 1990), this can be attributed to minor image blur.

5.3. Reading 3 (At 45.0°C)

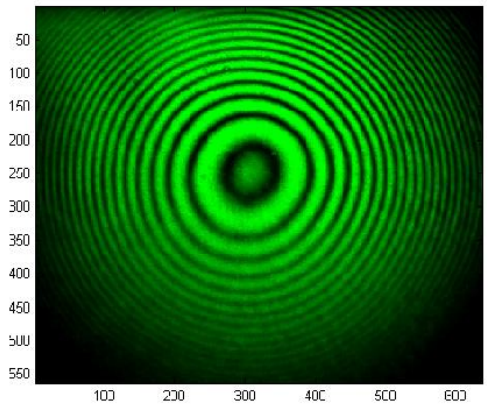

Fig. 14. Perturbed interference pattern.

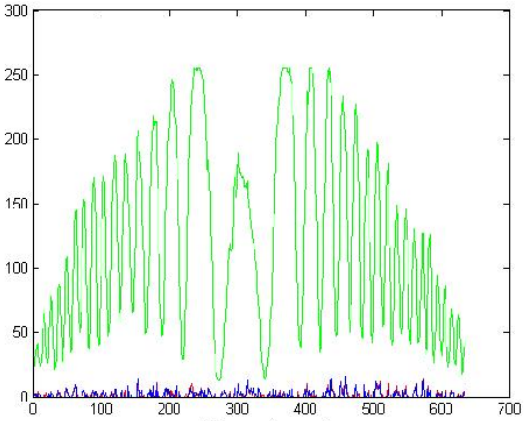

Fig. 16. Intensity profile at 45°C.

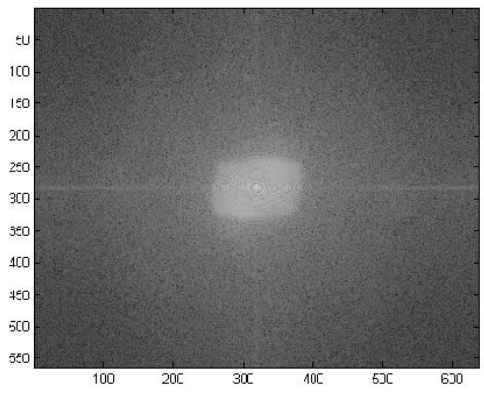

Fig. 15. The magnitude of the FFT.

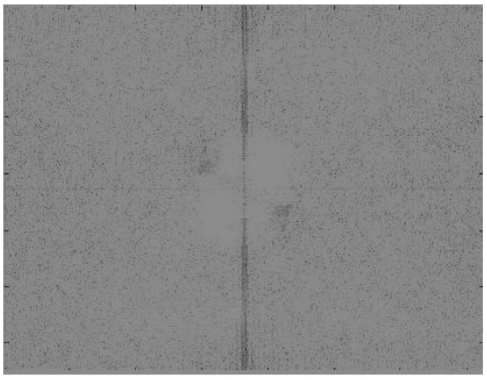

Fig. 17. Image subtraction of reading 3 from 1.

Reading 3 is conducted at 45°C, 21.9°C above room temperature within the turbulent region. The interferogram shows signs of distortion, defocus and blurring. The intensity profile still assumes a Gaussian profile with minor energy

redistribution between 100 and 150 units. The lower spatial frequencies are beginning to darken, which indicates that phase shifts are becoming more distinct with the increasing temperature. The darker line running down Figure 17 shows a redistribution of the spatial domain in the interferogram which corresponds to both image blur and image defocus. Work by (Banish, 1990) describes a similar scenario, which has been inferred in this work.

5.4. Reading 4 (At 55.0°C)

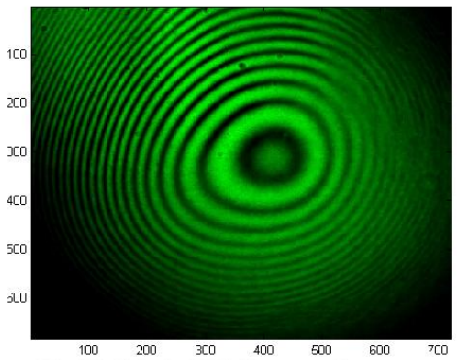

Fig. 18. Perturbed interference pattern.

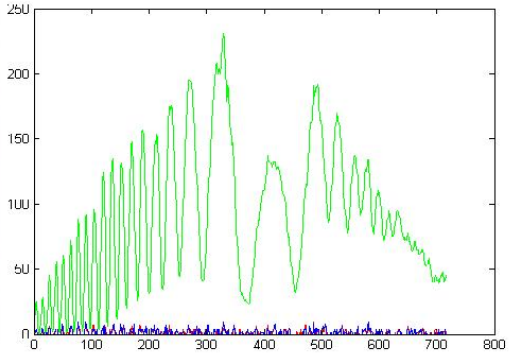

Fig. 20. Intensity profile at 55°C.

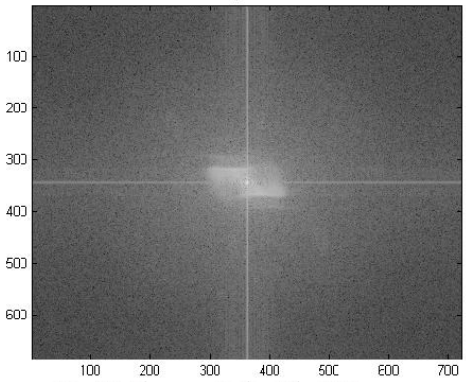

Fig. 19. The magnitude of the FFT.

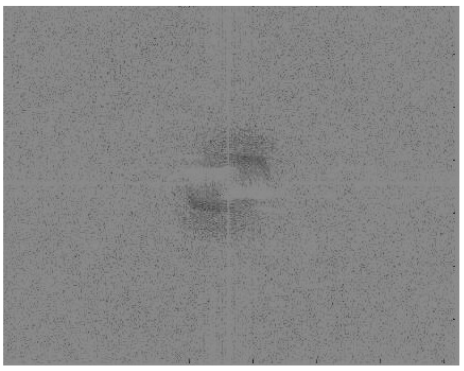

Fig. 21. Image subtraction of reading 4 from 1.

Reading 4 is 31.9°C above room temperature inside the turbulent region. The interferogram shows signs of deformity at the centroid and non-uniformity between the spacing of the nodes and anti-nodes. A phenomena described by (An-

drews *et al*, 1998) is evident here and is known as beam jitter, which describes the movement of the beam around the unperturbed region. The lower spatial frequencies do not coincide well with the original unperturbed FFT. This implies defocus and image blurriness (Banish, 1990) which can be directly seen from the interferogram. This could be a result of a redistribution of power spatially in time due to the thermal fluctuations (Shaik, 1989). Energy redistribution over the beam is severe over the region 500 to 700 units, with an overall maximum energy peak of less than 250 units. This redistribution of beam energy is known as beam spread (Andrews *et al*, 1998).

5.5. Reading 5 (At 65.0°C)

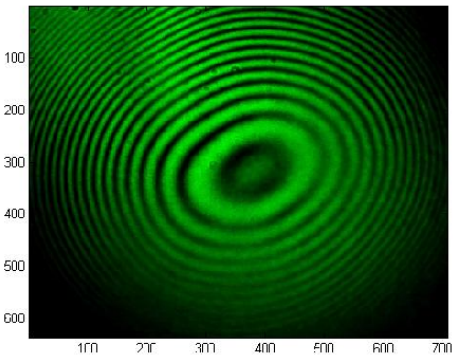

Fig. 22. Perturbed interference pattern.

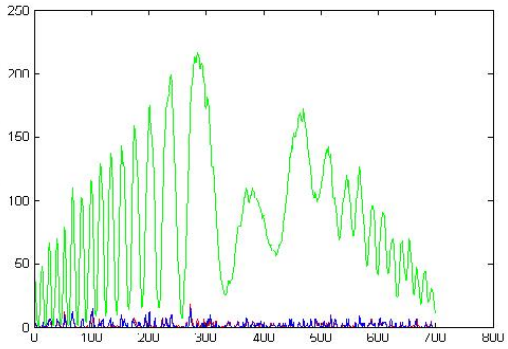

Fig. 24. Intensity profile at 65°C.

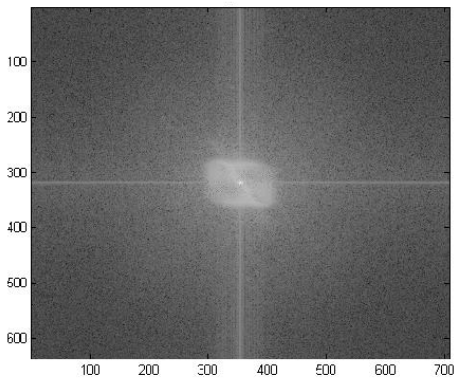

Fig. 23. The magnitude of the FFT.

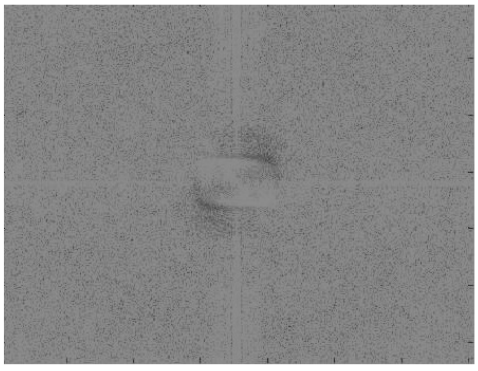

Fig. 25. Image subtraction of reading 5 from 1.

Reading 5 presents the results of the extreme temperature achievable using the heated panel. At 65°C, the laser beam is exposed to thermal heat radiating at 41.9°C above room temperature. The interferogram shows signs of image blurring , defocus and shape distortion (beam jitter). The intensity profile, however, provides a clearer understanding of energy redistribution over the beam. The maximum energy peak has decreased from a possible 250 units to an approximate value of 220 units. The energy redistribution (beam spreading) is considerable over the region of 400 and 700 units, and displays random non uniform energy peaks. An explanation for this could be described through the use of the image subtraction data. A darker region around the centre is evident when compared to previous data, which implies a larger lower spatial frequency redistribution. The implication of this is that it leads to increased defocus and image blur which has already been determined visually from the interferogram analysis (Banish, 1990). To classify the turbulence effect at various temperatures, the refractive index structure function was calculated and the results displayed in Table 3.

6. Determination of C_n^2

From equation 2, we can determine the turbulence strength due to a variation of temperature. A series of 5 readings were taken between two reference points $r = 0.2$ m apart. Readings 1-5 were taken at temperature values starting at approximately 30°C and ending at approximately 60°C with 5°C intervals. Before C_n^2 can be determined, the temperature structure function C_T^2 is required. This may be determined by invoking equation 3. Table 3 describes the temperature structure function C_T^2 and the turbulence strength C_n^2 with

separation $r = 0.2\,\mathrm{m}$. The data obtained for C_n^2 ranges in magnitude from

Reading	$C_T^2\,(K^2\,\mathrm{m}^{-2/3})$	$C_n^2\,(\times 10^{-12}\,\mathrm{m}^{-2/3})$
1	1.35	1.11
2	1.73	1.42
3	2.37	1.94
4	2.81	2.29
5	3.29	2.69

Table 3. Results of the turbulence strength C_n^2 for $r = 0.2\,\mathrm{m}$.

$1.1 \times 10^{-12}\,\mathrm{m}^{-2/3}$ to $2.7 \times 10^{-12}\,\mathrm{m}^{-2/3}$ which can be classified under the strong turbulence regime (Banish, 1990). Previous work by (Ndlovu, 2013) has described an environment of very weak turbulence within the turbulent region using a similar experimental setup to ours. His results are undoubtedly due to a fractional area being heated by the cigarette lighter source (Ndlovu, 2013). Although the flame produces intense temperatures, the focus of the heat is over a minuscule area. The turbulence generator used in our experiment provided a more consistent temperature delivery over a much larger region. Additionally in our work, slight variations in pressure were recorded which allowed for the precise calculation of C_T^2, the temperature structure function. (Ndlovu, 2013) neglected to account for this in his work and it seems to have also contributed to his lower C_T^2 values.

Typical values of C_n^2 for the atmosphere are 4 to 5 orders of magnitude larger than those obtained by(Ndlovu, 2013) and compare more favourably to the C_T^2 values determined in our work (Gamo, 1978 and Gochelashvili and Shishov, 1974). Previously published values of C_n^2 vary drastically from one source to another and are debatable (Gamo, 1978 and Gochelashvili

and Shishov, 1974). In the open atmosphere, path lengths extend over vast distances and in order for turbulent effects to be realised, the turbulence model must generate stronger turbulence. This fact is evident as shown by the Rytov variance with $\sigma_R^2 = 1.4 \times 10^{-3}$. For short propagation distances, as achieved in the laboratory, Gaussian beam propagation requires the condition of $\sigma_R^2 \leq 1$ for weak turbulence effects. The achieved scintillation therefore describes a weak turbulent environment despite the strong refractive index coefficient and this discrepancy can be attributed to the relatively short propagation paths. Figure 7 presents a graph of C_n^2 vs temperature for a separation distance of $r = 0.2\,\text{m}$.

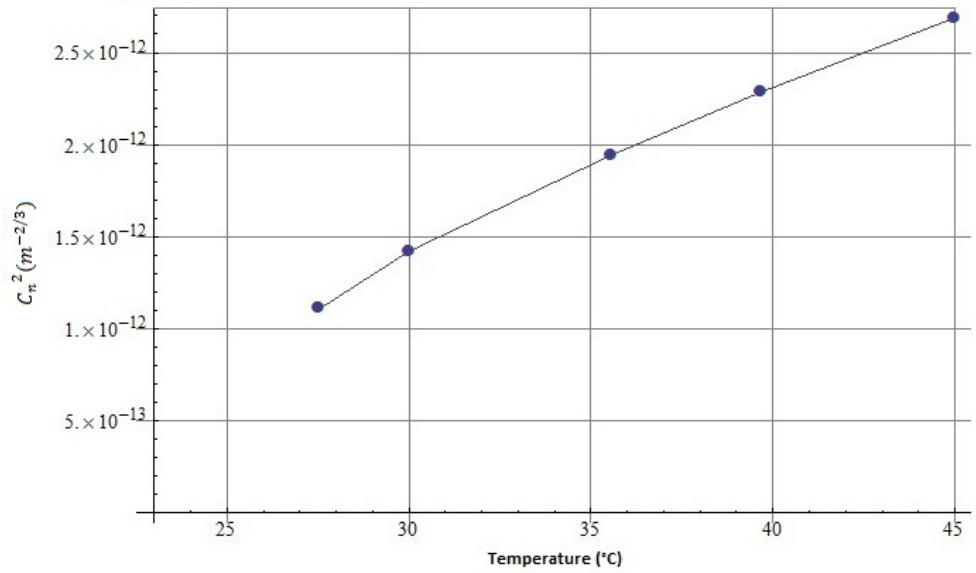

Fig. 7. Graph of C_n^2 vs Temperature with separation distance of $r = 0.2\,\text{m}$.

6.1. Comparison of C_n^2 data from various publications

Table 4 presents the refractive index structure constants C_n^2 from various published data. As previously explained, the values vary from one source to the

other and their relevance is highly interpretive for the specific condition. Numerous factors such as wind speed, humidity and mean temperature need to be considered before the data can be directly compared to our work. We are able to however immediately ascertain a common trend in this work and all comparative data - C_n^2 is temperature dependent. To graphically analyse and verify this trend, it may be necessary to plot a few scenarios of C_n^2 vs temperature from various sources.

$C_n^2\,(\mathrm{m}^{-2/3})$ range	Reference
$1.1\times\ 10^{-12}$ - 2.6×10^{-12}	This work
1.0×10^{-9} - 1.8×10^{-7}	(Wright and Schutz, 1967)
6.0×10^{-16} - 3.0×10^{-15}	(Weichel, 1990)
5.7×10^{-12} - 4.2×10^{-10}	(Magee, 1993)
2.0×10^{-16} - 4.5×10^{-14}	(Tunick *et al*, 2005)
2.5×10^{-19} - 1.1×10^{-17}	(Ndlovu, 2013)
$(3.3\pm0.15)\times10^{-8}$	(Ngo Nyobe *et al*, 2014)

Table 4. Comparison of results for C_n^2 with temperature.

Varying values of C_n^2 are tabulated in Table 4. The higher values of C_n^2, as described by (Ngo Nyobe *et al*, 2014), describe highly turbulent atmosphere and predict a high level of visual blurring such as the wavy lines one may encounter when looking at a hot metal surface. Lower values of C_n^2 as described by (Ndlovu, 2013), indicate more adiabatic conditions such as when it is windy or cloudy.

Figure 8 is a plot of C_n^2 versus temperature as obtained by (Magee, 1993) experimentally. (Magee, 1993), introduced a turbulent environment within a turbulence chamber in the laboratory and measured the perturbed wavefront using a shearing interferometer which allows direct comparison to be made with our

own results.

Temperature (°C)	$C_n^2\,(\times 10^{-12}\,\mathrm{m}^{-2/3})$
27	5.7
35	23.0
49	170.0
73	420.0

Table 5. Comparisons of results for C_n^2 with temperature.

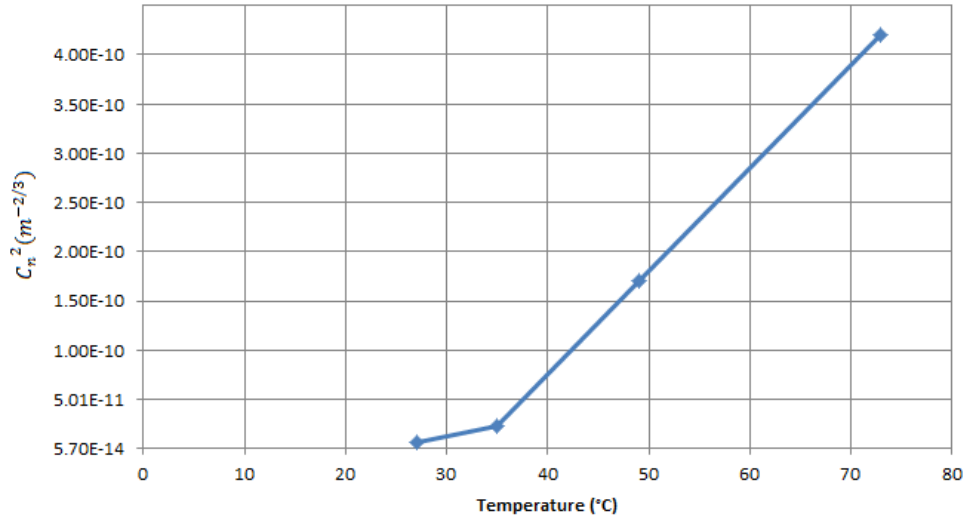

Fig. 8. Graph of C_n^2 vs Temperature (Magee, 1993).

Figure 7 and 8, although having different measurement scales, display similar patterns at higher temperatures. The difference in scales are attributed to the large turbulence chamber used by (Magee, 1993). His chamber provided consistent heating over a much larger path length than ours and his chamber fully surrounded the beam whilst ours did not. The different scales could also be due to the pressure and humidity fluctuations which contribute to the temperature structure function. Our results are very pleasing when considering that the

equipment used by (Magee, 1993) is highly specialised and very expensive. The major advantage of our work is the ability to reproduce equivalent results but still remaining robust and highly cost efficient.

Another interesting set of comparative results is that of (Weichel, 1990) in which the refractive index structure constant was determined at varying altitudes. Measurements began at ground level to a height of approximately 3 km above ground level. Restricting ourselves to a region of 300 m within the troposphere for analysis reasons, a plot of C_n^2 versus altitude is presented in Figure 9. The data provided by (Weichel, 1990) does not include temperature values at altitude and therefore a standard atmosphere calculator (Kroo, 1997) has been used to calculate approximate temperatures.

Altitude (m)	Temperature(°C)	$C_n^2\,(\times 10^{-15}\,\mathrm{m}^{-2/3})$
1	14.99	3.0
3	14.98	2.0
10	14.94	1.5
30	14.80	1.0
100	14.35	0.6
300	13.05	0.6

Table 6. Comparison of results for C_n^2, temperature and altitude.

The results although different from this work is useful for comparison since the troposphere describes our region of interest. It is the most active in terms of wind sheer, humidity and displays a decrease in temperature with respect to altitude. Figure 9 describes an increase in C_n^2 in relation to altitude. This is expected since for decreasing values of temperature, a decrease in C_n^2 is also predicted.

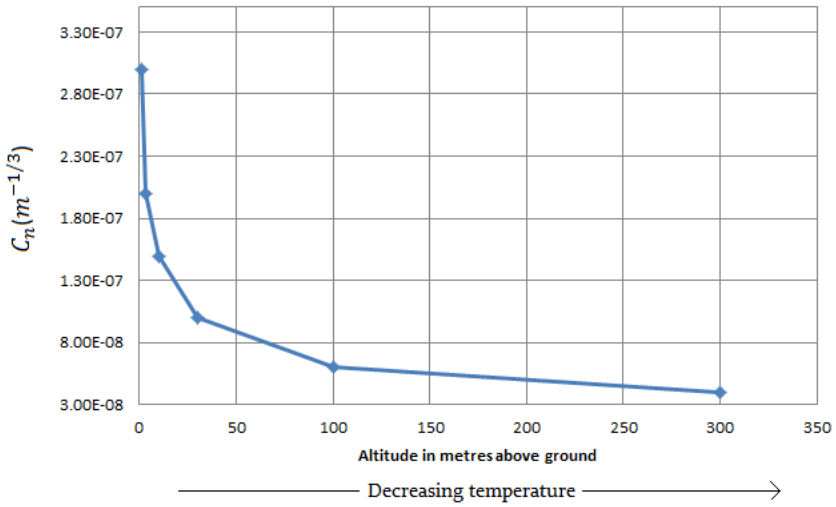

Fig. 9. Graph of C_n^2 vs Altitude (Weichel, 1990).

6.2. Error analysis

The statistical error in our work has been minimised by averaging results for C_n^2 (approximately 500 values were averaged for a single C_n^2 value as quoted in Table 3). The values for C_n^2 varied by less than 0.5% and thus may be neglected. Some experimental error analysis is also necessary. The accuracy of the PDI controller is quoted at 95% hence a maximum error of 5% can be expected for the turbulence generator. The pressure sensor quotes a maximum possible error of 0.1 Pa or a 1% error. The thermocouple states a precision of 0.1 °C which is approximately a 1% error. The total experimental error can be estimated at approximately 7% and hence a new C_n^2 range can be rewritten as $(1.89 \pm 0.64) \times 10^{-12}\,\mathrm{m}^{-2/3}$.

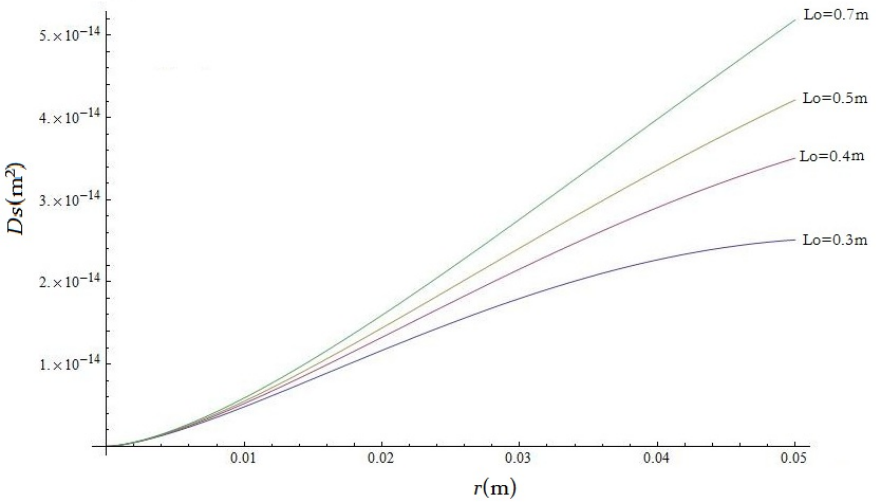

Fig. 10. Graph of the phase structure function $D_s(r)$ as a function of L_0.

6.3. The phase structure function $D_s(r)$

Figure 10 presents the phase structure function as a function of the outer scale L_0. The separation of the inner and outer scales is represented by r which typically varies between $1\,\text{mm} \leq r \leq 10\,\text{mm}$ (Kerr, 1972). An increase in the outer scale directly relates to an increase in the geometric structure function. This relation was proved by (Kerr, 1972) and shown by (Ndlovu, 2013) to have a similar trend.

The atmospheric coherence diameter was also determined to be $r_0 = 22\,\text{cm}$ which falls within 10% of accepted published values (Magee, 1993). For the high atmosphere observatories and in the presence of good seeing conditions, a value of $r_0 = 20\,\text{cm}$ can be achieved. Due to ground level positioning of the laboratory, optical seeing conditions are much weaker due to the high convective nature of the atmosphere. As a result, optical perturbations of the laser beam increase hence causing an increase in the optical coherence

diameter.

7. Conclusion

Unique modifications have been applied to an existing system to measure the effects of thermal turbulence on a laser beam. The laboratory experiment used a PDI to measure the thermal turbulence effects on a propagating laser beam in air. Analysis of the produced interferograms required the use of Fast Fourier Transforms to decompose the interferograms into their constituent magnitude and phase regimes. It has been previously discussed that the magnitude regime is of great importance, since it reveals the majority of the analysis data from the image. The data expressed for the laser beam at a room temperature of 23.1°C and represents the baseline for all comparisons. The data analysis revealed that a mere increase of 11.9°C provided substantial evidence that the laser beam experienced, although minor, directional fluctuations as well as image blur. Later data at higher thermal turbulence showed that the severity of intensity and directional fluctuations increased in accordance with temperature increases. This result fares well with the Rytov approximation which indicates that for weak turbulence, an increase in temperature leads to intensity fluctuations. The laboratory measured data, namely temperature structure function, refractive index structure function, scintillation and Fried's parameter, were also determined and are comparable to numerous published data. Each source varies drastically, which is acceptable since small changes in path length or temperature affect calculated data drastically. According to data of C_n^2, the turbulence strength resembles very strong conditions but, due to the short propagation length, the scintillation contradicts this result. The environment falls within the

very weak turbulence regime since $\sigma_R^2 \leq 1$. A coherence diameter of 22 cm was determined in the laboratory which does not fall within the range of 5-20 cm, since the seeing conditions at ground level are bad due to many factors such as weather and the highly turbulent nature of the atmosphere. Thus, we have effectively setup and tested a robust, inexpensive, highly accurate experiment to detect the effect of thermal turbulence on a propagating laser beam in air using a point diffraction interferometer. Future work consists of changing the turbulent source to include a heated wind stream which provides heat through a high velocity medium. Also of interest will be to move the entire setup to longer propagation distances in an open environment. A different choice of laser may also be necessary to examine the extent to which other lasers are affected. Such results are useful in defence weapon technology and are therefore sought after by many researchers.

References and Links

Andrews L. and Ronald P., *Laser Beam Propagation Through Random Media*, (Academic, Washington, 1998).

Andrews L.C., Phillips R.L., Sasiela R.J. and Parenti R., "Beam wander effects on the scintillation index of a focused beam", Proc.SPIE **5793**, (2005).

Baak T., "Thermal Coefficient of Refractive Index of Optical Glasses," J. Opt. Soc. Amer. **59**(7), 851-857 (1969).

Banish M. R., R.L. Clark and A.D. Kathman, "Wavelength dependence of blur circle size through turbulent flow", Window and Dome Technologies and Materials II, Proc. of SPIE **1326**, 196-206 (1990).

Berman G.P., Chumak A.A. and Gorshkov V. N., *Beam Wandering in the Atmosphere:The Effect of Partial Coherence*, (Academic, Ukraine, 2013).

Chatterjee R.M. and Fathi H.A.M., "Investigation of profiled beam propagation through a turbulent layer and temporal statistics of diffracted output for a modified von Karman phase screen," Proc. SPIE **897102**, 897102-897102-16 (2014).

Chernov L.A., *Wave Propagation in a Random Media*, (Academic, New York, 1967).

Churnside J.H and Lataitis R.J., "Wander of an optical beam in the turbulent atmosphere", Appl. Opt. **29**, 926-930 (1990).

Esposito R., "Power scintillations due to the wandering of the laser beam", *Proc. IEEE* **55**, 1533-1534 (1967).

Federico D., Juan A.R., Alejandro R. and Adolfo C., "Scintillation and beam-wander

analysis in an optical group station-satellite uplink," Applied Optics **43**(19), 3866-3873 (2004).

Gamo H. and Majumdar A.K., "Atmospheric turbulence chamber for transmission experiment: characterisation by thermal method," Appl. Opt., **17**, 3755-3762 (1978).

Gochelashvili K. and Shishov V., "Saturated Intensity Fluctuations of Laser Radiation in a Turbulent Medium," Zh. Eksp. Teor. Fiz **66**, 1237-1247 (1974).

Ibrahim A.T., "Using Microwave Energy To Treat Tumors", Progress In Electromagnetic Research B **3**, 1-27 (2007).

Ishimaru A., "Theory of Optical Propagation in the Atmosphere," Opt. Eng. **20**(1), 200163 (1981).

Kerr J.R., "Experiments on turbulence characteristics and multiwavelength scintillation phenomena," J. Opt. Soc. Am., **62**, 1040 (1972).

Kroo I., "Standard Atmosphere Calculator", *Aircraft Aerodynamics and Design Group*,16 April 1997. Web. 3 August 2014.

Lonappen A., Bindu G., Thomas V., Jacob J., Rajasekaran C. and Mathew K.T., "Diagnosis of Diabetes Mellitus Using Microwaves", Journal of Electromagnetic Waves and Applications **21**, 10 (2007).

Magee E.P., *Characterisation of Laboratory Generated Turbulence*, MSc Thesis, Air Force Institute of Technology, United States (1993).

Manderbach T.S., PhD thesis, Ludwig–Maximilians–Universitat Munchen (2007).

Mead J.B. and McIntosh R.E., "Millimeter-wave polarimetric radars", Progress In Elec-

tromagnetics Research, PIER 03, 391-450 (1990).

Ndlovu S., *Experimental Measurement of the Fluctuations of Laser Beam Due to Thermal Turbulence*, MSc thesis, University of Natal, South Africa (2013).

Ngo Nyobe E., Pemha E., Hona J., Bilong II J. and Lamara M., "Measurement of the structure coefficient of refractive index fluctuations in a turbulent premixed butane-air flame by means of a laser-based interferometer technique." *Optics and Lasers in Engineering*, **59**, 41-49 (2014).

Ojo J.S., Ajewole M.O. and Sarkar S.K., "Rain rate and rain attenuation prediction for satellite communication in Ku and Ka bands over Nigeria", Progress In Electrodynamics Research B **5**, 207-223 (2008).

Prod'homme L., "A new approach to the Thermal Change in the Refractive Index of Glasses," Phys. and Chem. of Glasses **1**(4), 119-122 (1969).

Shaik K.S., "Atmospheric Propagation Effects Relevant to Optical Communications," Communications Systems research Section (1988).

Shin R.T. and Kong J.A, "Radiative transfer theory for active remote sensing of two-layer random medium", Progress In Electromagnetics Research, PIER 01, 359-417 (1989).

Strohbehm J.W., *Laser Beam Propagation In The Atmosphere*, (Academic, New York, 1978).

Tatarskii V.I., "Wave Propagation in a Turbulent Medium Translated From Russian by R. A. Silverman and McGraw-Hill", (1961).

Titterton D.H., "The Development of Infrared Countermeasure Technology and Systems", Mid IR Semiconductor Optronic, Springer-Verlag, (2005).

Titterton P.J., “Power reduction and fluctuations caused by narrow laser beam motion in the far field”, Appl. Opt. **12**, 420-425 (1973).

Tunick A.,Tikhonov N., Vorontsov M. and Carhart G., *Characterisation of optical turbulence (Cn2) data measured at the ARL A_LOT facility*, US Army Research Laboratory, (2005).

Weichel H., *Laser Beam Propagation in the Atmosphere*, (Academic, Washington, 1990).

Wright, N. J. and Schutz, R. J., *Measuremetn of the refractive index structure coefficient Cn*, (No. BRL-MR-1885), Army ballistic research lab Aberdeen proving ground MD., (1967).

APPENDIX B

The graph below describes the phase structure function as a function of the outer scale L_0 and separation distance r.

- **Phase structure function:** $D_s = 2.91 * C_n^2 \, r^{5/3} \, z\left(1 - 0.8\left(\frac{2\pi r}{L_0}\right)^{1/3}\right)$
- **r - separation between l_0 and L_0**
- **z - propagation path length**
- **C_n^2 - refractive index structure function**
- **L_0 – outer scale**

In[1]:=
```
z = 2.523;
Cn2 = 2.6873*^-12;
Plot[{2.91 * (Cn2) * r^(5/3) * z * (1 - 0.8 * ((2 * π * r) / 0.3)^(1/3)),
  2.91 * (Cn2) * r^(5/3) * z * (1 - 0.8 * ((2 * π * r) / 0.4)^(1/3)),
  2.91 * (Cn2) * r^(5/3) * z * (1 - 0.8 * ((2 * π * r) / 0.5)^(1/3)),
  2.91 * (Cn2) * r^(5/3) * z * (1 - 0.8 * ((2 * π * r) / 0.7)^(1/3))},
 {r, 0, 0.1, .05}, AxesLabel → {r[m], D_s[m^2]}]
```

Out[3]=

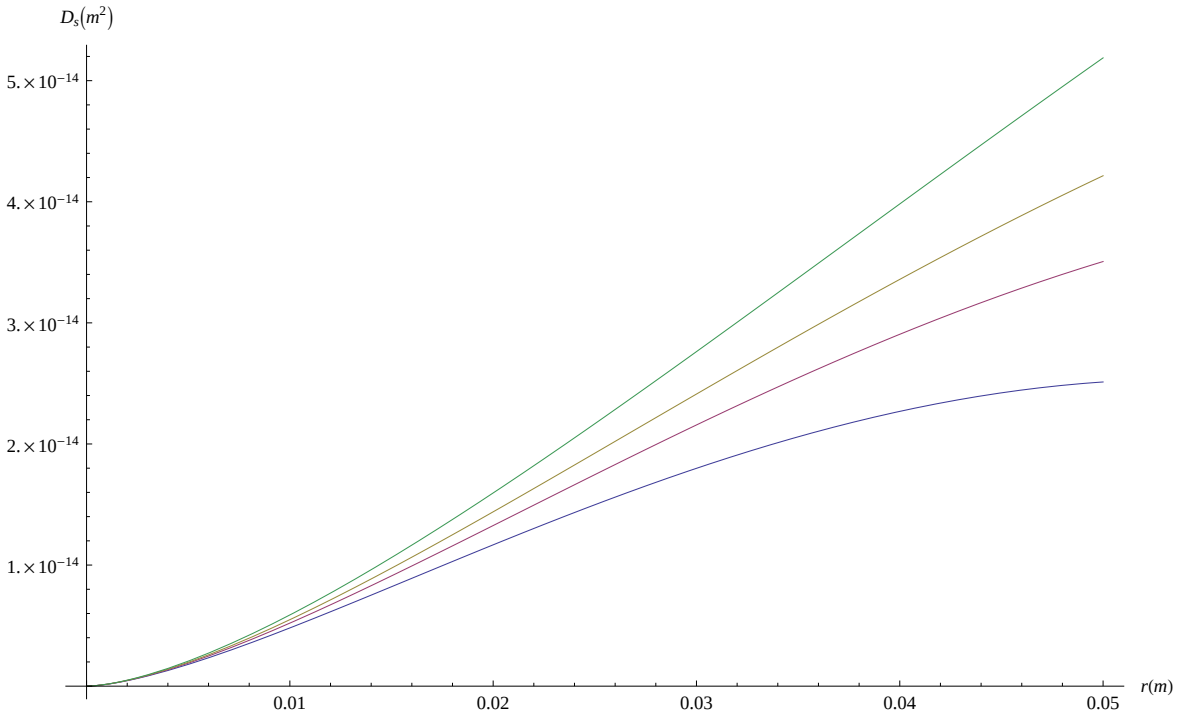

Fried's parameter is calculated as follows:

- **Seeing parameter**

In[4]:=
```
z = 2.523;
Cn2 = 2.6873*^-12;
λ = .5 * 10^-6;
```

In[7]:=
$$f = 0.185 \left(\frac{\lambda^2}{\text{Integrate}[Cn2 * e, \{e, 0, z\}]} \right)^{\frac{3}{5}} * 1000$$

Out[7]=
```
22.2159
```